JOURNAL OF GUIDANCE, CONTROL, AND DYNAMICS
Vol. 31, No. 4, July–August 2008

Carrier-Phase Differential Global Positioning System Navigation Filter for High-Altitude Spacecraft

Shan Mohiuddin* and Mark L. Psiaki†
Cornell University, Ithaca, New York 14853-7501

DOI: 10.2514/1.33948

A new navigation Kalman filter has been developed which uses carrier-phase differential Global Positioning System techniques in a framework that includes integer ambiguities to estimate the relative states of high-altitude, formation-flying spacecraft. This model-based approach to relative navigation allows spacecraft formations to use carrier-phase techniques above the Global Positioning System constellation. The filter uses dynamics models for the spacecraft orbits, receiver clocks, ionospheric total electron content, and Global Positioning System satellite residual position and clock errors. The process noise driving the orbital dynamics is separated into a common-mode part and lower intensity differential-mode part to better model how disturbances influence formations. The ionospheric total electron content model contains information that allows the filter to decide when to use the dual-frequency measurements to correct for the ionosphere and when to use them to aid in integer ambiguity resolution. The filter tracks undifferenced carrier-phase ambiguities, but still resolves the double-differenced integer ambiguities for use in the relative navigation solution. Monte Carlo simulations are used to evaluate the filter's performance. In geostationary scenarios, the filter's mean relative position error magnitude is 1.2 cm, and its maximum error magnitude is 6 cm. In high-Earth-orbit scenarios at an apogee distance of 18 Earth radii, the filter's mean error magnitude is 11 cm, and its maximum error magnitude is 54 cm. The correct integer ambiguities are resolved in one or two 30 s measurement steps in most cases.

I. Introduction

FORMATION flying of spacecraft is a key component in many space mission concepts. Formation-based sensing, for certain types of missions, can be more cost effective, redundant, flexible, and evolvable than single platform sensing that yields similar performance. Formation flying, however, is technically challenging, requiring each satellite to perform autonomous and accurate relative navigation. Carrier-phase differential Global Positioning System (CDGPS) techniques offer the required level of autonomy and accuracy, especially when combined with dynamics models through filtering. CDGPS techniques take the precise, but biased, Global Positioning System (GPS) carrier-phase measurements, resolve the biases through integer estimation techniques, and retain accurate information about the relative states of a pair of receivers. These techniques have already been demonstrated for low-Earth-orbit (LEO) spacecraft relative positioning in simulations [1–4] and in offline processing of flight data [5], achieving subcentimeter-level accuracy. This project applies CDGPS techniques to formations flying in geostationary orbits (GEO) and high-altitude Earth orbits (HEO), both of which require GPS receivers to operate above the GPS constellation. The orbits under consideration in this study are illustrated in Fig. 1.

A navigation system designed to work in high-altitude orbits must overcome several significant challenges. First, because the GPS receivers will be operating outside of the main broadcast beams of most of the GPS satellites, they must acquire and track the weak side lobes of the broadcast signals. It is assumed in this study that weak-signal GPS receivers that use the techniques in [6,7] are available. Second, the integer nature of the double-differenced carrier-phase measurement ambiguities can be corrupted if significant amounts of ionospheric total electron content (TEC) remain after the CDGPS differencing operations for GPS signals whose ray paths pass near the Earth. Differential TEC must be estimated, and its effects must be removed to resolve the ambiguities as exact integers, a necessary step for precise relative navigation. Third, poor geometric dilution of precision (GDOP) and slow line-of-sight (LOS) vector dynamics between the receivers and the GPS satellites make the integer ambiguities weakly observable, hindering the estimator's ability to resolve the values on the fly. Powerful integer-constrained linear least-squares estimation techniques, typically called LAMBDA/integer-linear-least-squares techniques (LAMBDA/ILLS), must be optimally integrated into the solution algorithm to overcome this challenge.

Although the high-altitude environment is challenging, it offers at least one advantage that is unavailable closer to Earth. The GPS receivers in high-altitude orbits will operate almost entirely outside of the ionosphere. Because the GPS satellites also operate outside of the ionosphere, many cases arise in which a broadcast signal's ray path never passes through a dense portion of the ionosphere. The effects of the differential TEC on that signal may be neglected. If the receiver-Earth-transmitter relative geometry is considered, such cases may be predicted, eliminating the need for the estimator to use the dual-frequency measurements to remove the effects of the ionosphere. The estimator is thus free to use those measurements for other important purposes, as will be discussed next. A realistic model of the magnitude and evolution of the TEC effects, therefore, could result in a more flexible estimator that makes multimodal use of the dual-frequency measurements.

Most of the previous research related to using CDGPS techniques for the relative navigation of satellite formations has focused on LEO applications. Researchers have used a variety of techniques, including single- and dual-frequency pointwise estimators [1,2] and single- and dual-frequency extended Kalman filters [3–5], to achieve centimeter- or subcentimeter-level relative position accuracy in simulations and in postprocessing of flight data. These algorithms benefit from the good signal environment and fast LOS vector dynamics found at low altitudes and cannot be directly applied to high-altitude formation scenarios. Other researchers have extended the use of CDGPS techniques to high altitudes [8,9], but only in the

Presented as Paper 6797 at the AIAA Guidance, Navigation, and Control Conference and Exhibit, Keystone, CO, 21–24 August 2006; received 8 August 2007; accepted for publication 30 November 2007.

*Graduate Student, Sibley School of Mechanical and Aerospace Engineering. AIAA Student Member.

†Professor, Sibley School of Mechanical and Aerospace Engineering. AIAA Associate Fellow.

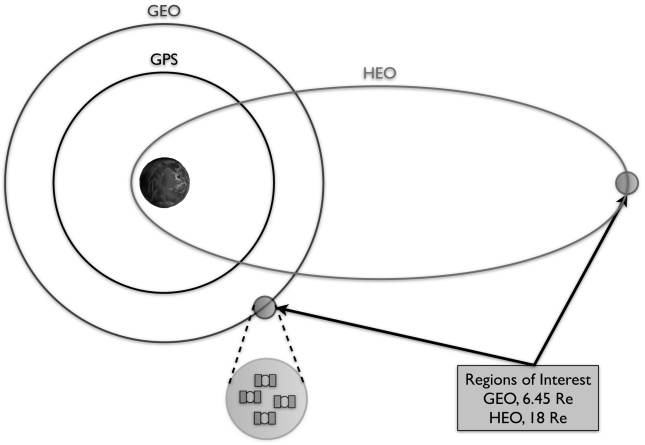

Fig. 1 Relative navigation scenarios.

context of pointwise estimation. These high-altitude pointwise estimators, however, suffer relatively large errors in the weakly observable radial direction, they do not produce velocity estimates, and they do not estimate TEC, or they use simplistic estimation techniques that include little a priori TEC knowledge.

The goal of this paper is to improve high-altitude relative navigation performance by using dual-frequency techniques and Kalman filtering techniques that exploit dynamics models. This research approaches this task in two steps. First, the single-frequency pointwise estimation techniques used in [8], and the GPS satellite residual position and clock error estimation techniques used in [9], are integrated into an extended Kalman filter. The filter augments its states to include spacecraft velocities and receiver clock rates. The coupling of the radial and along-track directions through the orbital dynamics, and the inclusion of receiver clock dynamics models, improves the relative position accuracy, especially in the radial direction, which is the direction with the largest errors [2,8]. The second step is to include dual-frequency measurements and a realistic dynamics model for the TEC, with special attention given to identifying those situations in which the differential TEC is significant and those in which it can be neglected. This model gives the filter the information it needs to decide whether to use the dual-frequency measurements to estimate and remove the effects of the ionosphere or to aid in integer ambiguity resolution through implicit wide laning.

The remainder of the paper is divided into five major sections. Section II describes the filter's dynamics models; Sec. III presents the carrier-phase and pseudorange measurement models; Sec. IV defines the Kalman filter algorithm; Sec. V evaluates the filter's performance using truth-model simulation results; Sec. VI gives the conclusions.

II. Dynamics Modeling

Three different relative navigation estimators (an L1-L2 filter, an L1-only filter, and an L1-only pointwise estimator) have been developed and are compared later in this paper.[‡] All three have been derived using similar techniques, but only the derivation of the L1-L2 filter is presented here. Where appropriate, the differences among these estimators are pointed out. The L1-L2 relative navigation filter is implemented in two steps: the propagation step and the measurement update step. The dynamics models for the propagation step are presented in this section, and the measurement equations for the measurement update step are presented in the next section. This paper focuses on the relative navigation of a pair of satellites, although the techniques are applicable to formations of an arbitrary number of spacecraft.

The propagation step is based on dynamics models for the orbits of the individual spacecraft, for the independent receiver clocks, for the GPS satellite residual position and clock errors, for the TEC along the LOS vectors from each receiver to each GPS satellite, and for the carrier-phase measurement ambiguities. The pointwise estimator includes limited dynamics models: a Markov model for the net LOS effect of the GPS spacecraft residual position and clock errors, and a constant model for the ambiguities. The L1 filter includes the same models as the L1-L2 filter, but does not model or estimate TEC.

The L1-L2 relative navigation filter uses absolute orbital dynamics models for each spacecraft. These models include a 2×2 gravity model and sun and moon disturbances. The nonlinear, continuous-time equations that describe the motion of an Earth-orbiting satellite are expressed in six states for each spacecraft with additive process noise.

$$\begin{bmatrix} \dot{\mathbf{X}}_{\mathrm{sc}_A}(t) \\ \dot{\mathbf{X}}_{\mathrm{sc}_B}(t) \end{bmatrix} = \begin{bmatrix} \mathbf{F}[\mathbf{X}_{\mathrm{sc}_A}(t), t] \\ \mathbf{F}[\mathbf{X}_{\mathrm{sc}_B}(t), t] \end{bmatrix} + D(t)\mathbf{w}_{\mathrm{sc}}(t) \tag{1}$$

The state vector contains the position and velocity of each satellite expressed in Earth-centered inertial (ECI) coordinates, and the function F includes the nonlinear accelerations of the satellite. The following equations are presented for user spacecraft A, but the same equations apply for spacecraft B.

$$\mathbf{X}_{\mathrm{sc}_A}(t) = \begin{bmatrix} x_A(t) \\ y_A(t) \\ z_A(t) \\ \dot{x}_A(t) \\ \dot{y}_A(t) \\ \dot{z}_A(t) \end{bmatrix}; \qquad \mathbf{F}[\mathbf{X}_{\mathrm{sc}_A}(t), t] = \begin{bmatrix} \dot{x}_A(t) \\ \dot{y}_A(t) \\ \dot{z}_A(t) \\ g_x[\mathbf{X}_{\mathrm{sc}_A}(t), t] \\ g_y[\mathbf{X}_{\mathrm{sc}_A}(t), t] \\ g_z[\mathbf{X}_{\mathrm{sc}_A}(t), t] \end{bmatrix} \tag{2}$$

where the functions g_x, g_y, and g_z are gravitational accelerations that include sun and moon effects.

The spacecraft state process noise vector $\mathbf{w}_{\mathrm{sc}}$ in Eq. (1) is modeled as a zero-mean, Gaussian perturbation to the spacecraft accelerations. The noise is divided into two parts, one that is common to both satellites and one that affects each satellite differentially. The relative proximity of the formation satellites in the much larger orbit indicates that each satellite's motion is governed mostly by the same influences. Only a small portion of the perturbations to the nominal dynamics affects the satellites differentially. By separating the process noise into a larger common-mode noise and a smaller differential-mode noise, the physical situation of relative navigation is better modeled. The process noise vector and its coefficient matrix used to achieve the separation are

$$\mathbf{w}_{\mathrm{sc}}(t) = \begin{bmatrix} \mathbf{w}_{AB}(t) \\ \delta\mathbf{w}_{AB}(t) \end{bmatrix}; \qquad D(t) = \begin{bmatrix} 0 & 0 \\ I & I \\ 0 & 0 \\ I & -I \end{bmatrix} = \begin{bmatrix} D_A \\ D_B \end{bmatrix} \tag{3}$$

where $\mathbf{w}_{AB}(t)$ is the common-mode process noise and $\delta\mathbf{w}_{AB}(t)$ is the much lower intensity differential-mode process noise. The process noise acceleration vectors for each spacecraft are thus defined as $\mathbf{w}_A(t) = \mathbf{w}_{AB}(t) + \delta\mathbf{w}_{AB}(t)$ and $\mathbf{w}_B(t) = \mathbf{w}_{AB}(t) - \delta\mathbf{w}_{AB}(t)$.

The discrete time version of the orbital dynamics model takes the form

$$\begin{aligned} \mathbf{x}_{\mathrm{sc}_k} &= \begin{bmatrix} \mathbf{X}_{\mathrm{sc}_A}(t_k) \\ \mathbf{X}_{\mathrm{sc}_B}(t_k) \end{bmatrix} = \mathbf{f}_{\mathrm{sc}}\left(\begin{bmatrix} \mathbf{X}_{\mathrm{sc}_A}(t_{k-1}) \\ \mathbf{X}_{\mathrm{sc}_B}(t_{k-1}) \end{bmatrix}, \mathbf{w}_{\mathrm{sc}_{K-1}}, t_{k-1} \right) \\ &= \mathbf{f}_{\mathrm{sc}}(\mathbf{x}_{\mathrm{sc}_{k-1}}, \mathbf{w}_{\mathrm{sc}_{k-1}}, t_{k-1}) \end{aligned} \tag{4}$$

where this equation also serves to define the dual-spacecraft discrete time state vector $\mathbf{x}_{\mathrm{sc}_k}$ at sample time t_k. The discrete time nonlinear dynamics function $\mathbf{f}_{\mathrm{sc}}$ that is used in Eq. (4) is evaluated by integrating the continuous-time dynamics in Eq. (1) from time t_{k-1} to time t_k using the zero-order hold assumption on the process noise.

$$\begin{bmatrix} \mathbf{w}_{AB}(t) \\ \delta\mathbf{w}_{AB}(t) \end{bmatrix} = \mathbf{w}_{\mathrm{sc}_{k-1}} \quad \text{for } t_{k-1} \le t < t_k \tag{5}$$

The linearized version of Eq. (4) takes the form

[‡]In this paper, "L1" refers to standard civilian GPS signal broadcast at 1575.42 MHz, and "L2" refers to the new civilian GPS signal broadcast at 1227.60 MHz that is being added to the system as part of GPS modernization.

$$\mathbf{x}_{\mathrm{sc}_k} = \mathbf{f}_{\mathrm{sc}}(\hat{\mathbf{x}}_{\mathrm{sc}_{k-1}}, 0, t_{k-1}) + \Phi_{\mathrm{sc}_{k-1}}(\mathbf{x}_{\mathrm{sc}_{k-1}} - \hat{\mathbf{x}}_{\mathrm{sc}_{k-1}}) + \Gamma_{\mathrm{sc}_{k-1}}\mathbf{w}_{\mathrm{sc}_{k-1}} \tag{6}$$

where $\hat{\mathbf{x}}_{\mathrm{sc}_{k-1}}$ is the nominal state at time t_{k-1}. The state transition matrix and the process noise influence matrix associated with Eq. (6), both of which are required for the Kalman filter algorithm [10], take the form

$$\Phi_{\mathrm{sc}_{k-1}} = \begin{bmatrix} \Phi_{\mathrm{sc}_A}(t_k, t_{k-1}) & 0 \\ 0 & \Phi_{\mathrm{sc}_B}(t_k, t_{k-1}) \end{bmatrix}; \quad \Gamma_{\mathrm{sc}_{k-1}} = \begin{bmatrix} \Gamma_{\mathrm{sc}_A}(t_k, t_{k-1}) \\ \Gamma_{\mathrm{sc}_B}(t_k, t_{k-1}) \end{bmatrix} \tag{7}$$

where Φ_{sc_A} and Γ_{sc_A} are determined by integrating continuous-time matrix differential equations that are derived from the spacecraft A part of Eq. (1), and where Φ_{sc_B} and Γ_{sc_B} are similarly derived from the spacecraft B part of Eq. (1). The associated process noise covariance is

$$Q_{\mathrm{sc}_{k-1}} = \begin{bmatrix} \frac{\beta_{w_{AB}}}{\Delta t_{k-1}} I & 0 \\ 0 & \frac{\beta_{\delta w_{AB}}}{\Delta t_{k-1}} I \end{bmatrix} \tag{8}$$

where I is a 3×3 identity matrix, $\beta_{w_{AB}}$ is the common-mode process noise intensity tuning parameter, and $\beta_{\delta w_{AB}}$ is the much smaller differential-mode tuning parameter.

The receiver clock errors are modeled as evolving according to a two-state random process for each receiver. This model is based on the model presented in [11]. The states are the clock error and the clock error rate. They are both expected to be random walk/drift processes during operation. The following are definitions of the clock model for receiver A, and similar definitions apply for receiver B.

$$\mathbf{x}_{\mathrm{clk}_{A_k}} = \begin{bmatrix} c\delta t_{A_k} \\ c\dot{\delta} t_{A_k} \end{bmatrix}; \quad \Phi_{\mathrm{clk}_{A_{k-1}}} = \begin{bmatrix} 1 & \Delta t_{k-1} \\ 0 & 1 \end{bmatrix}; \quad \mathbf{w}_{\mathrm{clk}_{A_{k-1}}} = \begin{bmatrix} w_{\delta t_{A_{k-1}}} \\ w_{\dot{\delta} t_{A_{k-1}}} \end{bmatrix} \tag{9}$$

Here, $c\delta t_{A_k}$ is the range equivalent receiver clock correction, $c\dot{\delta} t_{A_k}$ is the range rate equivalent receiver clock drift, Δt_{k-1} is the time step, $w_{\delta t_{A_{k-1}}}$ is the receiver clock drift process noise, and $w_{\dot{\delta} t_{A_{k-1}}}$ is the receiver clock frequency drift process noise. The models for both receiver clocks are combined.

$$\mathbf{x}_{\mathrm{clk}_k} = \begin{bmatrix} \underline{x}_{\mathrm{clk}_{A_k}} \\ \underline{x}_{\mathrm{clk}_{B_k}} \end{bmatrix}; \quad \Phi_{\mathrm{clk}_{k-1}} = \begin{bmatrix} \Phi_{\mathrm{clk}_{A_{k-1}}} & 0 \\ 0 & \Phi_{\mathrm{clk}_{B_{k-1}}} \end{bmatrix}; \quad \mathbf{w}_{\mathrm{clk}_{k-1}} = \begin{bmatrix} \mathbf{w}_{\mathrm{clk}_{A_{k-1}}} \\ \mathbf{w}_{\mathrm{clk}_{B_{k-1}}} \end{bmatrix} \tag{10}$$

The clock dynamics mapping for the two-receiver system can be written compactly as

$$\mathbf{x}_{\mathrm{clk}_k} = \Phi_{\mathrm{clk}_{k-1}}\mathbf{x}_{\mathrm{clk}_{k-1}} + \mathbf{w}_{\mathrm{clk}_{k-1}} \tag{11}$$

The associated process noise covariance is

$$Q_{\mathrm{clk}_{AB_{k-1}}} = \begin{bmatrix} S_f \Delta t_{k-1} + \frac{S_g \Delta t_{k-1}^3}{3} & \frac{S_g \Delta t_{k-1}^2}{2} \\ \frac{S_g \Delta t_{k-1}^2}{2} & S_g \Delta t_{k-1} \end{bmatrix}; \quad S_f = \frac{h_0}{2}; \quad S_g = 2\pi^2 h_{-2} \tag{12}$$

$$Q_{\mathrm{clk}_{k-1}} = \begin{bmatrix} Q_{\mathrm{clk}_{AB_{k-1}}} & 0 \\ 0 & Q_{\mathrm{clk}_{AB_{k-1}}} \end{bmatrix} \tag{13}$$

where the covariance is expressed in terms of the typical Allen variance parameters, h_0 and h_{-2}, for a temperature compensated crystal oscillator.

The GPS satellite residual position and clock errors, often referred to as ephemeris errors, are modeled as though they evolve according to a first-order Markov process to capture the expected time correlation of these errors. The vector of errors is defined as

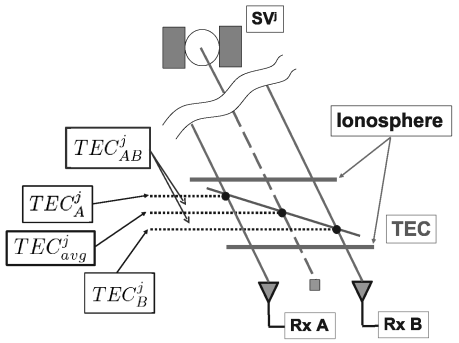

Fig. 2 Ionosphere model that separates the TEC into average values and differential values. The diagonal line represents the electron density profile across the portion of the ionosphere that is under consideration.

$\mathbf{e}_k = [\, e_k^1 \quad e_k^2 \quad \ldots \quad e_k^J \,]^T$, where e_k^j is the linear combination of the jth GPS satellite's residual position error projected onto the receiver-transmitter LOS vector plus the GPS satellite's distance-equivalent residual clock error. The number of commonly tracked GPS satellites is assumed to be J. The first-order Markov process mapping is

$$\mathbf{e}_k = \alpha_{e_{k-1}}\mathbf{e}_{k-1} + \Gamma_{e_{k-1}}\mathbf{w}_{e_{k-1}} \tag{14}$$

where

$$\alpha_{e_{k-1}} = \exp[-\Delta t_{k-1}/\tau_e] \tag{15}$$

$$\Gamma_{e_{k-1}} = (\sigma_e \sqrt{1 - \exp[-2\Delta t_{k-1}/\tau_e]})I \tag{16}$$

In this model, the vector $\mathbf{w}_{e_{k-1}}$ is an element of a zero-mean, unit-variance, discrete-time, white-process-noise sequence, τ_e is the Markov correlation time constant, σ_e is the steady-state standard deviation for each element in $\mathbf{e}$, and I is a $J \times J$ identity matrix. The process noise covariance for the ephemeris errors $Q_{e_{k-1}}$ is equal to the $J \times J$ identity matrix because the intensity scaling is already included in the dynamics mapping.

The ionospheric TEC values are also modeled as evolving according to a first-order Markov process to capture their expected time correlations. The model also captures the expected spacial correlation between receivers operating relatively close to one another by dividing the TEC values experienced by a pair of receivers into two parts: an average part, also called the common-mode part, and a differential part.

$$\mathrm{TEC}_A^j = \mathrm{TEC}_{\mathrm{avg}}^j + \mathrm{TEC}_{AB}^j \tag{17}$$

$$\mathrm{TEC}_B^j = \mathrm{TEC}_{\mathrm{avg}}^j - \mathrm{TEC}_{AB}^j \tag{18}$$

where TEC_A^j is the TEC along the LOS from receiver A to GPS satellite j, and where TEC_B^j applies for receiver B and GPS satellite j. Here, $\mathrm{TEC}_{\mathrm{avg}}^j$ is the average TEC between the two receivers, and TEC_{AB}^j is the differential TEC. These definitions are illustrated in Fig. 2.

The average and differential TEC terms for the J commonly tracked GPS satellites are assembled into the following vector of unknowns:

$$\mathbf{T}_k = \begin{bmatrix} \mathbf{T}_{\mathrm{avg}_k} \\ \mathbf{T}_{AB_k} \end{bmatrix} \tag{19}$$

where

$$\mathbf{T}_{\mathrm{avg}_k} = [\, \mathrm{TEC}_{\mathrm{avg}_k}^1 \quad \mathrm{TEC}_{\mathrm{avg}_k}^2 \quad \ldots \quad \mathrm{TEC}_{\mathrm{avg}_k}^J \,]^T \tag{20}$$

$$\mathbf{T}_{AB_k} = [\, \mathrm{TEC}_{AB_k}^1 \quad \mathrm{TEC}_{AB_k}^2 \quad \ldots \quad \mathrm{TEC}_{AB_k}^J \,]^T \tag{21}$$

These state definitions allow the noise intensities for the average and differential TEC to be tuned separately in the following TEC dynamics mapping:

$$\mathbf{T}_k = \alpha_{T_{k-1}} \mathbf{T}_{k-1} + \underbrace{\begin{bmatrix} \beta_{T_{\text{avg}_{k-1}}} & 0 \\ 0 & \beta_{T_{AB_{k-1}}} \end{bmatrix}}_{\Gamma_{T_{k-1}}} \mathbf{w}_{T_{k-1}} \tag{22}$$

where the vector $\mathbf{w}_{T_{k-1}}$ is an element of a zero-mean, unit-variance, white-process-noise sequence. The state mapping and average TEC noise intensity scaling are defined as

$$\alpha_{T_{k-1}} = \exp[-\Delta t_{k-1}/\tau_T] \tag{23}$$

$$\beta_{T_{\text{avg}_{k-1}}} = (\sigma_{T_{\text{avg}}} \sqrt{1 - \exp[-2\Delta t_{k-1}/\tau_T]}) I \tag{24}$$

where τ_T is the correlation time constant, $\sigma_{T_{\text{avg}}}$ is the steady-state standard deviation for the average TEC values, and I is a $J \times J$ identity matrix.

Before discussing the differential TEC noise intensity scaling $\beta_{T_{AB_{k-1}}}$, an important distinction between low-altitude and high-altitude CDGPS must be made. At low altitudes, all GPS receivers operate below or inside the ionosphere, and the received signals all pass through a significant portion of the ionosphere. Under these conditions, the effects of TEC can only be neglected when the baseline distances between the receivers are sufficiently small so that the differential TEC, the part that influences the relative navigation solution, approaches zero. In GEO and above, many of the received signals never pass through any significant portion of the ionosphere. In these cases, the effects of the differential ionosphere will be very small, even over large baseline distances. When the signal's ray path does enter a dense portion of the ionosphere, which is the case when a GPS satellite is rising or setting, large TEC gradients can produce large differential TEC, even for two receivers that are relatively close to one another. The differential TEC in these cases must be accurately estimated and removed to ensure accurate relative spacecraft state estimates.

The TEC first-order Markov process model incorporates this understanding of the physical situation into the differential TEC noise intensity scaling by considering the receiver-Earth-transmitter geometry. The differential TEC noise intensity scaling is

$$\beta_{T_{AB_{k-1}}} = (\sigma_{T_{AB}} \sqrt{1 - \exp[-2\Delta t_{k-1}/\tau_T]}) \begin{bmatrix} \frac{h_{\text{iono}}}{d^1_{\text{los}}} & & & \\ & \frac{h_{\text{iono}}}{d^2_{\text{los}}} & & \\ & & \ddots & \\ & & & \frac{h_{\text{iono}}}{d^J_{\text{los}}} \end{bmatrix} \tag{25}$$

The term h_{iono} is the height of the densest portion of the ionosphere, and the terms d^j_{los} for $j = 1, 2, \ldots, J$ are the minimum heights of the line-of-sight vectors above the Earth's surface, as defined in Fig. 3. As the jth GPS signal's ray path moves close to Earth, d^j_{los} approaches h_{iono}, and the ratio of these values approaches one. This scenario causes the worst-case noise intensity to be used in the model. Thus, the expected range of values for the differential TEC for channel j will be relatively large, and the filter will be aware of the need to estimate TEC^j_{AB}. On the other hand, as the ray path moves away from Earth, the ratio of h_{iono} to d^j_{los} becomes small, tightening the range of possible values for the differential TEC by reducing the noise intensity. In this situation, the differential TEC should be near zero, and the model informs the filter that an a priori estimate of $\text{TEC}^j_{AB} = 0$ is reasonable. Thus, by considering the receiver-Earth-transmitter relative geometry, the filter is aware of the situations in which the differential ionosphere is significant and those in which it is negligible. The process noise covariances for the average TEC $Q_{T_{\text{avg}}}$, and for the differential TEC $Q_{T_{AB}}$, are both equal to the $J \times J$ identity matrix because the intensity scalings are already included in the TEC dynamics mapping.

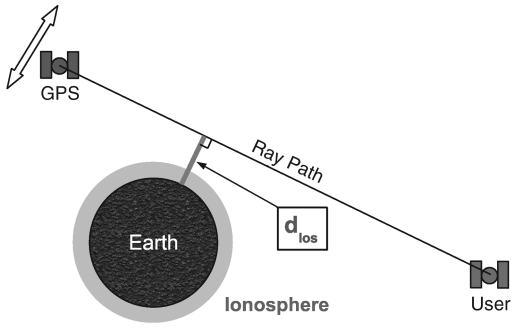

Fig. 3 Height of ray path above the Earth.

Note, it might be reasonable to use a similar altitude-dependent process noise influence for the average TEC values. This level of complexity was not thought worthwhile because of its negligible impact of the relative navigation accuracy.

The carrier-phase measurement ambiguities are modeled as being real-valued and exactly constant. They are defined in vector form as follows:

$$\mathbf{a} = \begin{bmatrix} \mathbf{a}_{1A} \\ \mathbf{a}_{1B} \\ \mathbf{a}_{2A} \\ \mathbf{a}_{2B} \end{bmatrix} \tag{26}$$

where

$$\mathbf{a}_{1A} = \begin{bmatrix} a^1_{1A} \\ a^2_{1A} \\ \vdots \\ a^J_{1A} \end{bmatrix}; \quad \mathbf{a}_{1B} = \begin{bmatrix} a^1_{1B} \\ a^2_{1B} \\ \vdots \\ a^J_{1B} \end{bmatrix}; \quad \mathbf{a}_{2A} = \begin{bmatrix} a^1_{2A} \\ a^2_{2A} \\ \vdots \\ a^J_{2A} \end{bmatrix}; \quad \mathbf{a}_{2B} = \begin{bmatrix} a^1_{2B} \\ a^2_{2B} \\ \vdots \\ a^J_{2B} \end{bmatrix} \tag{27}$$

In these definitions, the superscripts indicate the GPS satellite, the subscript numbers 1 or 2 indicate the GPS frequency L1 or L2, and the subscript letters A or B indicate the receiver. Although the ambiguities are real-valued, later developments will exploit the fact that certain differencing operations performed on these values will result in integers.

III. Measurement Equations

The measurement equations for the L1-L2 relative navigation filter are presented in this section. The filter uses pseudorange and carrier-phase measurements from the L1 and L2 GPS signals. The related L1 pointwise estimator and the related L1 filter only use measurements from the L1 GPS signal and do not estimate TEC.

The standard pseudorange equations are used. These are presented for receiver A at time t_k, although the same equations apply for receiver B. The k subscripts are suppressed for readability.

$$P^j_{1A} = \rho^j_A + c(\delta t_A - \delta t^j) + \text{TEC}^j_A + e^j + n^j_{1A_P} \tag{28}$$

$$P^j_{2A} = \rho^j_A + c(\delta t_A - \delta t^j) + \frac{f^2_{L1}}{f^2_{L2}} \text{TEC}^j_A + e^j + n^j_{2A_P} \tag{29}$$

Here, f_{L1} is the nominal L1 frequency, and f_{L2} is the nominal L2 frequency, P^j_{1A} and P^j_{2A} are the L1 and L2 measured pseudoranges from satellite j, ρ^j_A is the geometric range from satellite j, c is the speed of light in a vacuum, δt_A is the receiver clock offset, δt^j is the satellite clock correction, TEC^j_A is the range equivalent TEC at the L1 frequency, and $n^j_{1A_P}$ and $n^j_{2A_P}$ are the errors due to thermal noise and multipath in the L1 and L2 measurements. The carrier-phase measurement equations are based on the model developed in [12],

with the exception that the dependence on the GPS satellite clock correction coefficient a_{f1} is removed without sacrificing accuracy.

$$\lambda_{L1}\phi_{1A}^{j} = \rho_{A}^{j} + c(\delta t_A - \delta t^j) - \mathrm{TEC}_{A}^{j} + e^j + \lambda_{L1}a_{1A}^{j} + n_{1A_\phi}^{j} \quad (30)$$

$$\lambda_{L2}\phi_{2A}^{j} = \rho_{A}^{j} + c(\delta t_A - \delta t^j) - \frac{f_{L1}^2}{f_{L2}^2}\mathrm{TEC}_{A}^{j} + e^j + \lambda_{L2}a_{2A}^{j} + n_{2A_\phi}^{j} \quad (31)$$

where λ_{L1} is the nominal L1 carrier wavelength, λ_{L2} is the nominal L2 carrier wavelength, a_{1A}^{j} and a_{2A}^{j} are the real-valued L1 and L2 carrier-phase measurement ambiguities as defined in Eq. (27), and $n_{1A_\phi}^{j}$ and $n_{2A_\phi}^{j}$ are the errors due to thermal noise and multipath in the L1 and L2 measurements.

It is important to note that the ambiguities in these equations are not integers. Traditional data processing for CDGPS includes the explicit double-differencing of the carrier-phase measurements to achieve integers. Double-differenced processing results in correlated measurement errors, makes carrier-phase cycle slip detection and recovery difficult, and discards the knowledge that the real-valued, undifferenced ambiguities are constant. The algorithms in this study attempt to avoid these problems while still taking advantage of the integer nature of the double-differenced ambiguities. They do so in two steps. First, the estimators keep track of the undifferenced ambiguities, and they make sure that the error sources which could make these values appear to be time varying are estimated and removed. Such time-varying error sources include TEC and GPS ephemeris errors. Second, the algorithms exploit the integer nature of the double-differenced ambiguities by transforming the undifferenced ambiguities into double-differenced integer ambiguities during the measurement update step. These integers are estimated using LAMBDA/ILLS techniques and the estimates are used in the navigation solution. A inverse transformation recovers the undifferenced ambiguities without loss of information. These transformations, which were first developed in [9], are presented in the Sec. IV.

The traditional CDGPS data processing that explicitly differences the carrier-phase measurements also has the effect of restricting the ways in which the measurements can be used. It has been shown in [9] that dual-frequency measurements cannot be used simultaneously to do wide laning to aid in ambiguity resolution *and* to estimate and remove the effects of the ionosphere. In the traditional approach, the filter designer must choose between alternative differencing schemes to achieve these distinct goals and may decide to do wide laning and ionosphere removal in sequence. The approach used in this paper allows the filter to decide how best to use the dual-frequency measurements on a channel-by-channel basis and on the fly. This functionality is enabled by giving the filter undifferenced measurements and statistical models of the expected sources of measurement error. With this information, the filter can decide for itself how to weight the alternative types of implicit measurement differencing on a channel-by-channel basis. This "soft" differencing occurs during the square-root information data processing and will be discussed in the next section.

In the following measurement equations, the LOS ephemeris errors to a given GPS satellite are treated as being the same for each receiver at time t_k. An assumption underlies this treatment. It is assumed that the LOS vectors from a particular GPS satellite to the two receivers are similar enough that the projections of the ephemeris errors onto the those vectors are not significantly different. This assumption is reasonable for the types of formations under consideration in this study, but should be reconsidered if the baseline distances become very large, e.g., several hundreds of kilometers.

The measurement equations are linearized about the pseudorange solution at each receiver independently, a method that has proven robust and that encourages fast carrier-phase ambiguity resolution [8,9]. The linearized measurement equations for receiver A are

$$P_{1A}^{j} - \rho_{A_0}^{j} + c\delta t^j - (\hat{\boldsymbol{\rho}}_{A}^{j})^T\mathbf{r}_{A_0} = -(\hat{\boldsymbol{\rho}}_{A}^{j})^T\mathbf{r}_A + c\delta t_A + e^j + (\mathrm{TEC}_{\mathrm{avg}}^{j} + \mathrm{TEC}_{AB}^{j}) + n_{1A_P}^{j} \quad (32)$$

$$P_{2A}^{j} - \rho_{A_0}^{j} + c\delta t^j - (\hat{\boldsymbol{\rho}}_{A}^{j})^T\mathbf{r}_{A_0} = -(\hat{\boldsymbol{\rho}}_{A}^{j})^T\mathbf{r}_A + c\delta t_A + e^j + \frac{f_{L1}^2}{f_{L2}^2}(\mathrm{TEC}_{\mathrm{avg}}^{j} + \mathrm{TEC}_{AB}^{j}) + n_{2A_P}^{j} \quad (33)$$

$$\lambda_{L1}\phi_{1A}^{j} - \rho_{A_0}^{j} + c\delta t^j - (\hat{\boldsymbol{\rho}}_{A}^{j})^T\mathbf{r}_{A_0} = -(\hat{\boldsymbol{\rho}}_{A}^{j})^T\mathbf{r}_A + c\delta t_A + e^j - (\mathrm{TEC}_{\mathrm{avg}}^{j} + \mathrm{TEC}_{AB}^{j}) + \lambda_{L1}a_{A}^{j} + n_{1A_\phi}^{j} \quad (34)$$

$$\lambda_{L2}\phi_{2A}^{j} - \rho_{A_0}^{j} + c\delta t^j - (\hat{\boldsymbol{\rho}}_{A}^{j})^T\mathbf{r}_{A_0} = -(\hat{\boldsymbol{\rho}}_{A}^{j})^T\mathbf{r}_A + c\delta t_A + e^j - \frac{f_{L1}^2}{f_{L2}^2}(\mathrm{TEC}_{\mathrm{avg}}^{j} + \mathrm{TEC}_{AB}^{j}) + \lambda_{L2}a_{A}^{j} + n_{2A_\phi}^{j} \quad (35)$$

where $\rho_{A_0}^{j}$ is the pseudorange solution's range, $\hat{\boldsymbol{\rho}}_{A}^{j}$ is the pseudorange solution line-of-sight unit vector defined as pointing from receiver A to GPS satellite j, $\mathbf{r}_{A_0}$ is the pseudorange solution's position estimate defined as $\mathbf{r}_{A_0} = [\,x_{A_0}(t_k) \quad y_{A_0}(t_k) \quad z_{A_0}(t_k)\,]^T$, and $\mathbf{r}_A$ is the similarly defined true position of the spacecraft. Note, the similar equations apply for receiver B with the exception that the TEC values are $\mathrm{TEC}_{\mathrm{avg}}^{j} - \mathrm{TEC}_{AB}^{j}$, consistent with the definition given in Eq. (17). The linearization assumes the availability of four or more GPS signals for the purposes of calculating the pseudorange solution. It differs from the standard extended Kalman filter technique of linearizing about the a priori state estimate. It is possible, however, that the standard linearization method also would work well.

IV. Kalman Filter for Mixed Real/Integer States

The relative navigation solution is computed using a square-root information implementation of an extended Kalman filter [13]. This type of implementation is numerically stable and appropriate for use with linear integer estimation techniques that increase the convergence rates to the correct double-differenced carrier-phase ambiguities.

The information equations for the square-root information filter require the inverse square-root of the process noise covariance matrix to be computed. This covariance matrix is a large block matrix that has along its diagonal the individual covariance matrices for each component of the process noise. All of the individual covariance matrices have been defined in the dynamics modeling section. The square-root of the large process noise covariance matrix Q_{k-1} is computed by inverting the transpose of the Cholesky factorization. Thus,

$$R_{ww_{k-1}}^{-1}R_{ww_{k-1}}^{-T} = Q_{k-1} \quad (36)$$

where $R_{ww_{k-1}}$ is the desired process noise square-root information matrix.

The dynamics propagation begins by assembling the state and process noise information equations. These equations contain a priori square-root information matrices (SRIMs) and the associated square-root information vectors for each block that will be propagated. These include blocks for the spacecraft position, the velocity states and clock states (combined into one vector $\mathbf{x} = [\,\mathbf{x}_{\mathrm{sc}}^T \quad \mathbf{x}_{\mathrm{clk}}^T\,]^T$), the TEC states, the ephemeris error states, and the real-valued ambiguity states. Using standard square-root information filter (SRIF) techniques [13], the information equations take the following form:

$$\begin{bmatrix} 0 \\ \mathbf{z}_{x_{k-1}} \\ \mathbf{z}_{T_{k-1}} \\ \mathbf{z}_{e_{k-1}} \\ \mathbf{z}_{a_{k-1}} \end{bmatrix} = \begin{bmatrix} R_{ww} & 0 & 0 & 0 & 0 \\ 0 & R_{xx_{k-1}} & R_{xT_{k-1}} & R_{xe_{k-1}} & R_{xa_{k-1}} \\ 0 & 0 & R_{TT_{k-1}} & R_{Te_{k-1}} & R_{Ta_{k-1}} \\ 0 & 0 & 0 & R_{ee_{k-1}} & R_{ea_{k-1}} \\ 0 & 0 & 0 & 0 & R_{aa_{k-1}} \end{bmatrix} \begin{bmatrix} \mathbf{w}_{k-1} \\ \mathbf{x}_{k-1} \\ \mathbf{T}_{k-1} \\ \mathbf{e}_{k-1} \\ \mathbf{a} \end{bmatrix} + \begin{bmatrix} \mathbf{v}_{w_{k-1}} \\ \mathbf{v}_{x_{k-1}} \\ \mathbf{v}_{T_{k-1}} \\ \mathbf{v}_{e_{k-1}} \\ \mathbf{v}_{a_{k-1}} \end{bmatrix} \tag{37}$$

where the vectors $\mathbf{v}_{w_{k-1}}$, $\mathbf{v}_{x_{k-1}}$, $\mathbf{v}_{T_{k-1}}$, $\mathbf{v}_{e_{k-1}}$, and $\mathbf{v}_{a_{k-1}}$ are all elements of zero-mean, unit-variance, white-noise sequences that are uncorrelated with each other. Because the carrier-phase ambiguities are modeled as being exactly constant from time step to time step, it is not required to include them in the propagation step explicitly. Nevertheless, they are included here for completeness.

The dynamics models in Eqs. (6), (11), (14), and (22) are substituted into Eq. (37) to eliminate the state variables at time t_{k-1} in favor of the state variables at time t_k. The process noise vector $\mathbf{w}_{k-1}$, however, remains in the equation. The resulting equation is subjected to a standard SRIF factorization to produce the following a priori square-root information equation:

$$\begin{bmatrix} \bar{\mathbf{z}}_{w_{k-1}} \\ \bar{\mathbf{z}}_{x_k} \\ \bar{\mathbf{z}}_{T_k} \\ \bar{\mathbf{z}}_{e_k} \\ \bar{\mathbf{z}}_{a_k} \end{bmatrix} = \begin{bmatrix} \bar{R}_{ww_k} & \bar{R}_{wx_k} & \bar{R}_{wT_k} & \bar{R}_{we_k} & \bar{R}_{wa_k} \\ 0 & \bar{R}_{xx_k} & \bar{R}_{xT_k} & \bar{R}_{xe_k} & \bar{R}_{xa_k} \\ 0 & 0 & \bar{R}_{TT_k} & \bar{R}_{Te_k} & \bar{R}_{Ta_k} \\ 0 & 0 & 0 & \bar{R}_{ee_k} & \bar{R}_{ea_k} \\ 0 & 0 & 0 & 0 & \bar{R}_{aa_k} \end{bmatrix} \begin{bmatrix} \mathbf{w}_{k-1} \\ \mathbf{x}_k \\ \mathbf{T}_k \\ \mathbf{e}_k \\ \mathbf{a} \end{bmatrix} + \begin{bmatrix} \bar{\mathbf{v}}_{w_{k-1}} \\ \bar{\mathbf{v}}_{p_k} \end{bmatrix} \tag{38}$$

where $\bar{\mathbf{v}}_{p_k}$ is an element from a zero-mean, unit-variance, white-noise sequence. At this point, the a priori states could be calculated from Eq. (38) by setting $\bar{\mathbf{v}}_{p_k}$ equal to zero and solving by back substitution. This calculation, however, is not required because the measurement linearizations are carried out about the pseudorange solutions rather than the a priori state estimates.

The measurement update is performed next. For square-root information processing, the measurement noise must be characterized to precondition the measurement equations so that their Gaussian measurement noise vectors are zero-mean and unit-variance. The measurement error covariance matrices and their square-root inverse factorizations for the pseudorange and carrier-phase measurement equations are

$$P_P = \sigma_P^2 I = R_{vv_P}^{-1} R_{vv_P}^{-T} \tag{39}$$

$$P_\phi = \sigma_\phi^2 I = R_{vv_\phi}^{-1} R_{vv_\phi}^{-T} \tag{40}$$

where σ_P is the pseudorange measurement error standard deviation and σ_ϕ is the carrier-phase measurement error standard deviation.

The linearized measurements in Eqs. (32–35) are assembled into block form by repeating them for each available GPS satellite and for both receivers. The resulting blocks are each preconditioned by left multiplying them by the inverse square-root of the appropriate measurement noise covariance matrix from Eq. (39) or Eq. (40). The properly preconditioned measurement equations are written in the following form:

$$\mathbf{y}_k = H_{x_k}\mathbf{x}_k + H_{T_k}\mathbf{T}_k + H_{e_k}\mathbf{e}_k + H_{a_k}\mathbf{a} + \mathbf{n}_k \tag{41}$$

This equation is combined with the a priori information (omitting the process noise blocks) from the propagation step to give the following block form:

$$\begin{bmatrix} \mathbf{y}_k \\ \bar{\mathbf{z}}_{x_k} \\ \bar{\mathbf{z}}_{T_k} \\ \bar{\mathbf{z}}_{e_k} \\ \bar{\mathbf{z}}_{a_k} \end{bmatrix} = \begin{bmatrix} H_{x_k} & H_{T_k} & H_{e_k} & H_{a_k} \\ \bar{R}_{xx_k} & \bar{R}_{xT_k} & \bar{R}_{xe_k} & \bar{R}_{xa_k} \\ 0 & \bar{R}_{TT_k} & \bar{R}_{Te_k} & \bar{R}_{Ta_k} \\ 0 & 0 & \bar{R}_{ee_k} & \bar{R}_{ea_k} \\ 0 & 0 & 0 & \bar{R}_{aa_k} \end{bmatrix} \begin{bmatrix} \mathbf{x}_k \\ \mathbf{T}_k \\ \mathbf{e}_k \\ \mathbf{a} \end{bmatrix} + \underbrace{\begin{bmatrix} \mathbf{n}_k \\ \bar{\mathbf{v}}_{p_k} \end{bmatrix}}_{\bar{\mathbf{v}}_{m_k}} \tag{42}$$

where $\bar{\mathbf{v}}_{m_k}$ is a zero-mean, unit-variance noise vector implicitly defined in this equation.

Standard SRIF factorization techniques are used to transform Eq. (42) into the following block upper-triangular form:

$$\begin{bmatrix} \mathbf{z}_{x_k} \\ \mathbf{z}_{T_k} \\ \mathbf{z}_{e_k} \\ \mathbf{z}_{a_k} \\ \mathbf{z}_{r_k} \end{bmatrix} = \begin{bmatrix} R_{xx_k} & R_{xT_k} & R_{xe_k} & R_{xa_k} \\ 0 & R_{TT_k} & R_{Te_k} & R_{Ta_k} \\ 0 & 0 & R_{ee_k} & R_{ea_k} \\ 0 & 0 & 0 & R_{aa_k} \\ 0 & 0 & 0 & 0 \end{bmatrix} \begin{bmatrix} \mathbf{x}_k \\ \mathbf{T}_k \\ \mathbf{e}_k \\ \mathbf{a} \end{bmatrix} + \mathbf{v}_{m_k} \tag{43}$$

where $\mathbf{z}_{r_k}$ is the square-root information measurement residual vector.

The undifferenced, real-valued ambiguity block is isolated in Eq. (43), and a transformation is developed that separates the ambiguities on each frequency into irreducibly real elements and double-differenced integer elements. This transformation allows the integer parts to be resolved using powerful integer least-squares techniques. This transformation is equivalent to the one developed in [9]. The double-differenced integer ambiguities are defined as follows:

$$\mathbf{N} = \begin{bmatrix} (a_{1B}^2 - a_{1A}^2) - (a_{1B}^1 - a_{1A}^1) \\ (a_{1B}^3 - a_{1A}^3) - (a_{1B}^1 - a_{1A}^1) \\ \vdots \\ (a_{1B}^J - a_{1A}^J) - (a_{1B}^1 - a_{1A}^1) \\ (a_{2B}^2 - a_{2A}^2) - (a_{2B}^1 - a_{2A}^1) \\ (a_{2B}^3 - a_{2A}^3) - (a_{2B}^1 - a_{2A}^1) \\ \vdots \\ (a_{2B}^J - a_{2A}^J) - (a_{2B}^1 - a_{2A}^1) \end{bmatrix} = G\mathbf{a} \tag{44}$$

where G_k is a $2(J-1) \times 4J$ matrix of ones, negatives ones, and zeros arranged to produce $\mathbf{N}$, which is a $2(J-1) \times 1$ vector of double-differenced integer ambiguities. The transformation matrix is factorized into the product of a square, orthonormal matrix and an upper-triangular matrix, a factorization commonly called QR factorization [14], resulting in the following system:

$$\mathcal{Q}_1 \begin{bmatrix} R_1^T \\ 0 \end{bmatrix} = G^T \tag{45}$$

or transposing

$$[R_1 \quad 0]\mathcal{Q}_1^T = G \tag{46}$$

Here, $\mathcal{Q}_1$ is the orthonormal matrix and R_1^T is a square, nonsingular, upper-triangular matrix. This factorization may be used to define the following underdetermined set of equations for the real-valued ambiguities given the double-differenced ambiguities:

$$\mathbf{N} = [R_1 \quad 0]\mathcal{Q}_1^T\mathbf{a} \tag{47}$$

The underdetermined subspace of $\mathbf{a}$ can be defined as a vector of irreducibly real ambiguities $\mathbf{a}_{\text{ir}}$ that has dimension $2(J+1)$. The

relationship between this new vector $\mathbf{a}_{\text{ir}}$, the original vector $\mathbf{a}$, and the integer ambiguity vector $\mathbf{N}$ is

$$\begin{bmatrix}\mathbf{a}_{\text{ir}}\\ \mathbf{N}\end{bmatrix}=\begin{bmatrix}0 & I\\ R_1^T & 0\end{bmatrix}\mathcal{Q}_1^T\mathbf{a} \tag{48}$$

Solving for $\mathbf{a}$ yields

$$\mathbf{a}=\mathcal{Q}_1\begin{bmatrix}0 & R_1^{-T}\\ I & 0\end{bmatrix}\begin{bmatrix}\mathbf{a}_{\text{ir}}\\ \mathbf{N}\end{bmatrix}=E\begin{bmatrix}\mathbf{a}_{\text{ir}}\\ \mathbf{N}\end{bmatrix} \tag{49}$$

where the $2(J+1)\times 2(J+1)$ matrix E is implicitly defined by this equation.

To apply LAMBDA/ILLS methods to determine the optimal estimate of $\mathbf{N}$, it is necessary to develop an information equation that isolates $\mathbf{N}$ from the real-valued estimated states. This is done by using Eq. (49) to eliminate $\mathbf{a}$ from Eq. (43) in favor of the unknowns $\mathbf{a}_{\text{ir}}$ and $\mathbf{N}$. Afterward, the fourth row of the information equation is transformed using QR factorization to isolate an $\mathbf{N}$ information equation. The QR factorization and transformation to do this take the form

$$\mathcal{Q}_{2_k}\begin{bmatrix}R_{\text{iri}r_k} & R_{\text{ir}N_k}\\ 0 & R_{NN_k}\end{bmatrix}=R_{aa_k}E \tag{50}$$

$$\begin{bmatrix}\mathbf{z}_{\text{ir}_k}\\ \mathbf{z}_{N_k}\end{bmatrix}=\mathcal{Q}_{2_k}^T\bar{\mathbf{z}}_{a_k} \tag{51}$$

where $\mathcal{Q}_{2_k}$ is an orthonormal matrix, $R_{\text{iri}r_k}$ and R_{NN_k} are square, nonsingular, upper-triangular matrices, and $R_{\text{ir}N_k}$ is a dense matrix of appropriate dimensions. Some additional transformations that will aid in the computation of the state estimates and estimation error covariance matrices are performed:

$$\begin{bmatrix}R_{x\text{ir}_k} & R_{xN_k}\\ R_{T\text{ir}_k} & R_{TN_k}\\ R_{e\text{ir}_k} & R_{eN_k}\end{bmatrix}=\begin{bmatrix}R_{xa_k}\\ R_{Ta_k}\\ R_{ea_k}\end{bmatrix}E \tag{52}$$

At this point, the following a posteriori square-root information equation applies:

$$\begin{bmatrix}\mathbf{z}_{x_k}\\ \mathbf{z}_{T_k}\\ \mathbf{z}_{e_k}\\ \mathbf{z}_{\text{ir}_k}\\ \mathbf{z}_{N_k}\\ \mathbf{z}_{r_k}\end{bmatrix}=\begin{bmatrix}R_{xx_k} & R_{xT_k} & R_{xe_k} & R_{x\text{ir}_k} & R_{xN_k}\\ 0 & R_{TT_k} & R_{Te_k} & R_{T\text{ir}_k} & R_{TN_k}\\ 0 & 0 & R_{ee_k} & R_{e\text{ir}_k} & R_{eN_k}\\ 0 & 0 & 0 & R_{\text{iri}r_k} & R_{\text{ir}N_k}\\ 0 & 0 & 0 & 0 & R_{NN_k}\\ 0 & 0 & 0 & 0 & 0\end{bmatrix}\begin{bmatrix}\mathbf{x}_k\\ \mathbf{T}_k\\ \mathbf{e}_k\\ \mathbf{a}_{\text{ir}}\\ \mathbf{N}\end{bmatrix}+\mathbf{v}_{m_k} \tag{53}$$

where $\bar{\mathbf{v}}_{m_k}$ is the appropriately transformed zero-mean, unit-variance noise vector. Notice how the integer ambiguity states $\mathbf{N}$, in the lower, right-hand block of Eq. (53), are isolated from the real-valued states. This decoupling of the integer problem allows specialized techniques to be used to solve for $\mathbf{N}$.

The ambiguity SRIM R_{NN_k} and the ambiguity information vector $\mathbf{z}_{N_k}$ are passed to a decorrelation and integer linear least-squares solution algorithm which finds the $\mathbf{N}$ that minimizes

$$J(\mathbf{N})=\frac{1}{2}(R_{NN_k}\mathbf{N}-\mathbf{z}_{N_k})^T(R_{NN_k}\mathbf{N}-\mathbf{z}_{N_k}) \tag{54}$$

under the constraint that

$$\mathbf{N}\in Z^{2(J-1)} \tag{55}$$

where $Z^{2(J-1)}$ indicates the $2(J-1)$-dimensional integer vector space. The decorrelation part of this process is merely a preconditioning step that further transforms R_{NN_k} and $\mathbf{z}_{N_k}$ to expedite the integer least-squares optimization. Algorithms that perform this decorrelation and optimization are commonly referred to as LAMBDA/ILLS methods. For more information on the LAMBDA/ILLS algorithms used in this paper, please see [15].

Once the double-differenced integer ambiguities have been estimated,[§] the measurement update step is completed by calculating the remaining a posteriori state estimates via back substitution in Eq. (53):

$$\hat{\mathbf{a}}_{\text{ir}}=R_{\text{iri}r_k}^{-1}[\mathbf{z}_{\text{ir}_k}-R_{\text{ir}N_k}\mathbf{N}_{\text{opt}}] \tag{56}$$

$$\hat{\mathbf{e}}_k=R_{ee_k}^{-1}[\mathbf{z}_{e_k}-R_{e\text{ir}_k}\hat{\mathbf{a}}_{\text{ir}}-R_{eN_k}\mathbf{N}_{\text{opt}}] \tag{57}$$

$$\hat{\mathbf{T}}_k=R_{TT_k}^{-1}[\mathbf{z}_{T_k}-R_{Te_k}\hat{\mathbf{e}}_{k-1}-R_{T\text{ir}_k}\hat{\mathbf{a}}_{\text{ir}}-R_{TN_k}\mathbf{N}_{\text{opt}}] \tag{58}$$

$$\hat{\mathbf{x}}_k=R_{xx_k}^{-1}[\mathbf{z}_{x_k}-R_{xT_k}\hat{\mathbf{T}}_{k-1}-R_{xe_k}\hat{\mathbf{e}}_{k-1}-R_{x\text{ir}_k}\hat{\mathbf{a}}_{\text{ir}}-R_{xN_k}\mathbf{N}_{\text{opt}}] \tag{59}$$

The vectors $\mathbf{z}_{n_k}$, $\mathbf{z}_{T_k}$, $\mathbf{z}_{e_k}$, and $\mathbf{z}_{a_k}$ and the matrices R_{xx_k}, R_{xT_k}, R_{xe_k}, R_{xa_k}, R_{TT_k}, R_{Te_k}, R_{Ta_k}, R_{ee_k}, R_{ea_k}, and R_{aa_k} from Eq. (43) are all passed forward to the filter's next recursion for use in the dynamics propagation step. These square-root information vectors and matrices, however, are only valid if the measurements used in the filter's next recursion are taken from the same set of GPS satellites used in its current recursion. If any signals are added or dropped, then the square-root information vectors and matrices in Eq. (43) must be modified.

Consider the case where a new satellite is acquired on the pth channel. Seven new variables must be estimated: the average and differential total electron content along the signals' ray path $\text{TEC}_{\text{avg}}^p$ and TEC_{AB}^p; the new GPS satellite's ephemeris error e^p; and the real-valued, undifferenced ambiguities for each receiver and each GPS frequency a_{1A}^p, a_{2A}^p, a_{1B}^p, and a_{2B}^p. The state vector from Eq. (43) is augmented with these new variables, and the square-root information vectors and matrices from Eq. (43) are augmented to include a reasonable a priori square-root information equation for each new variable. For the TEC and ephemeris error variables, the new square-root information equations take the following form:

$$z_{T_{\text{avg}}}^p=\left(\frac{1}{\sigma_{T_{\text{avg}}}}\right)\text{TEC}_{\text{avg}}^p+v_{T_{\text{avg}}}^p \tag{60}$$

$$z_{T_{AB}}^p=\left(\frac{1}{\sigma_{T_{AB}}}\right)\text{TEC}_{AB}^p+v_{T_{AB}}^p \tag{61}$$

$$z_e^p=\left(\frac{1}{\sigma_e}\right)e^p+v_e^p \tag{62}$$

In these equations, the terms on the left-hand side, $z_{T_{\text{avg}}}^p$, $z_{T_{AB}}^p$, and z_e^p, are the a priori square-root information elements to be inserted into the existing square-root information vectors. The terms $\sigma_{T_{\text{avg}}}$, $\sigma_{T_{AB}}$, and σ_e are the expected standard deviations of the new variables, and the reciprocals of these terms, shown in parentheses in Eqs. (60–62), are the new diagonal elements to be inserted into the existing SRIMs. The terms $v_{T_{\text{avg}}}^p$, $v_{T_{AB}}^p$, and v_e^p are the new elements of the noise vectors.

The goal here is to provide the filter with appropriate a priori statistics for the new variables. This is done by choosing reasonable values for $z_{T_{\text{avg}}}^p$, $z_{T_{AB}}^p$, z_e^p, $\sigma_{T_{\text{avg}}}$, $\sigma_{T_{AB}}$, and σ_e based on the physics of the navigation problem. Because the TEC values in the high-altitude orbits are usually near zero, and because the ephemeris errors are

[§]Note: the Kalman filter should also validate its double-differenced integer ambiguity estimates. Validation is the process of determining whether the probability that $\mathbf{N}_{\text{opt}}$ is correct is sufficiently high to assume the value to be exact. For more information on ambiguity validation, please see [16]. At present, the Kalman filter does not perform a validation calculation. Given that it reestimates the integers at each measurement update, this can be an acceptable approach because it never strictly fixes the values of $\mathbf{N}$.

expected to be zero mean, a reasonable choice for the a priori values of $z^p_{T_{\text{avg}}}$, $z^p_{T_{AB}}$, and z^p_e is to set each equal to zero. The choice for the a priori standard deviation values is guided by the Markov models described previously. The maximum standard deviations in those models are used for $\sigma_{T_{\text{avg}}}$, $\sigma_{T_{AB}}$, and σ_e.

The square-root information equations for the remaining four new variables, the new ambiguities, take a similar form:

$$z^p_{a_{1A}} = \left(\frac{1}{\sigma_a}\right) a^p_{1A} + v^p_{a_{1A}} \tag{63}$$

This equation applies for the L1 ambiguity at receiver A, although similar equations apply for the L2 ambiguity at receiver A, and for the L1 and L2 ambiguities at receiver B. Because the new ambiguity in Eq. (63) can take on any value, the a priori uncertainty associated with it is infinite, i.e., $\sigma_a = \infty$. The infinite uncertainty indicates that $z^p_{a_{1A}}$ contains no useful information for the filter, and that it may, therefore, be set to an arbitrary value. Notice the assumption in Eqs. (60–63) that the new unknowns are uncorrelated with each other and with the previously estimated unknowns. This assumption makes augmenting the appropriate blocks in Eq. (43) a straightforward task.

Next, consider the case where the pth commonly tracked GPS satellite is dropped. The same seven variables discussed in the previous paragraphs and their associated square-root information equations are now discarded. The dropped variables, however, are not independent of the retained variables. In other words, the square-root information equations associated with the dropped variables also contain information about the retained variables. A procedure must be applied that separates the information that applies to the kept variables from the information that applies to the dropped variables, so that the latter may be discarded without losing useful information. This procedure involves three steps. First, the state vector is permuted to place the dropped variables at the top of the vector. This has the effect of reordering the columns of the large block upper-triangular SRIM in Eq. (43) such that the columns associated with the dropped variables are moved to the first seven columns of the matrix. The modified information equation, with the time index subscripts suppressed for readability, is

$$\begin{bmatrix} \mathbf{z}_x \\ \mathbf{z}_T \\ \mathbf{z}_e \\ \mathbf{z}_a \\ \mathbf{z}_r \end{bmatrix} = \begin{bmatrix} R_{xd} & R_{xx} & \tilde{R}_{xT} & \tilde{R}_{xe} & \tilde{R}_{xa} \\ R_{Td} & 0 & \tilde{R}_{TT} & \tilde{R}_{Te} & \tilde{R}_{Ta} \\ R_{ed} & 0 & 0 & \tilde{R}_{ee} & \tilde{R}_{ea} \\ R_{ad} & 0 & 0 & 0 & \tilde{R}_{aa} \\ 0 & 0 & 0 & 0 & 0 \end{bmatrix} \begin{bmatrix} \mathbf{d} \\ \mathbf{x} \\ \tilde{\mathbf{T}} \\ \tilde{\mathbf{e}} \\ \tilde{\mathbf{a}} \end{bmatrix} + \begin{bmatrix} \mathbf{v}_d \\ \tilde{\mathbf{v}}_{m_k} \end{bmatrix} \tag{64}$$

where

$$\mathbf{d} = \begin{bmatrix} \text{TEC}^p_{\text{avg}} \\ \text{TEC}^p_{AB} \\ e^p \\ a^p_{1A} \\ a^p_{2A} \\ a^p_{1B} \\ a^p_{2B} \end{bmatrix} \tag{65}$$

and where R_{xd}, R_{Td}, R_{ed}, and R_{ad} are constructed by taking the columns from Eq. (43) that are associated with the dropped variables and grouping them together. The tilde notation as applied to a SRIM indicates that the matrix has been modified by removing one or more of its columns. The tilde notation as applied to a state vector or a noise vector indicates that particular elements of the vector have been removed. The second step in the dropped satellite procedure is to decouple the information associated with the retained variables from the information associated with the dropped variables. This decoupling is accomplished by QR factorizing and transforming Eq. (64), resulting in the following block upper-triangular system:

$$\begin{bmatrix} \bar{\mathbf{z}}_d \\ \bar{\mathbf{z}}_x \\ \bar{\mathbf{z}}_T \\ \bar{\mathbf{z}}_e \\ \bar{\mathbf{z}}_a \\ \mathbf{z}_r \end{bmatrix} = \begin{bmatrix} \bar{R}_{dd} & \bar{R}_{dx} & \bar{R}_{dT} & \bar{R}_{de} & \bar{R}_{da} \\ 0 & \bar{R}_{xx} & \bar{R}_{xT} & \bar{R}_{xe} & \bar{R}_{xa} \\ 0 & 0 & \bar{R}_{TT} & \bar{R}_{Te} & \bar{R}_{Ta} \\ 0 & 0 & 0 & \bar{R}_{ee} & \bar{R}_{ea} \\ 0 & 0 & 0 & 0 & \bar{R}_{aa} \\ 0 & 0 & 0 & 0 & 0 \end{bmatrix} \begin{bmatrix} \mathbf{d} \\ \mathbf{x} \\ \tilde{\mathbf{T}} \\ \tilde{\mathbf{e}} \\ \tilde{\mathbf{a}} \end{bmatrix} + \begin{bmatrix} \bar{\mathbf{v}}_d \\ \bar{\mathbf{v}}_m \end{bmatrix} \tag{66}$$

The final step is to discard the first row of this equation and to extract the proper information vectors and matrices to pass forward to the next recursion. These vectors and matrices are taken from the second through fifth rows of Eq. (66). Note, if the double-differenced integer ambiguities for the dropped satellite had been validated, then a more complex satellite dropping procedure could have been developed to retain the information that is inherent in the validation. Also, the add/drop procedures described in this section have been presented for adding/dropping a single GPS satellite. The methods, however, may be applied recursively to handle adding/dropping multiple satellites.

V. Results

The relative navigation algorithms have been tested using Monte Carlo simulations. Each Monte Carlo run uses a high-fidelity truth-model simulation that replicates the output of GPS receivers' pseudorange and carrier-phase measurements in user-defined satellite formation scenarios. The offline MATLAB simulation algorithm is described in detail in [12]. It incorporates physics-based models of many error sources: the effects of the ionosphere and multipath; antenna phase-center variations and polarization-induced phase windup; receiver clock drift, thermal noise, and line biases; and GPS satellite ephemeris errors. For details about these error models, please consult [12].

Two template scenarios have been designed to test a filter's navigation performance in high-altitude orbits. The first consists of a two-spacecraft formation orbiting in GEO with a nominal baseline distance of 3 km. The simulated receivers are assumed to have the weak-signal acquisition and tracking capability described in [6,7]. Using such technology, receivers in GEO are assumed to be able to acquire and track signals with a C/N_0 as low as 18 dB · Hz. This level of sensitivity allows the receivers to track up to 12 GPS signals with GDOP values ranging between 5 and 15 [12]. These scenarios are referred to as the GEO scenarios. The second template scenario consists of a two-spacecraft formation near apogee in a 1.2×18 Earth radii orbit with a nominal baseline distance of 10 km. The simulated receivers are assumed to be able to track signals down to $C/N_0 = 12$ dB · Hz. This threshold allows the tracking of as many as 11 satellites at apogee with GDOP values ranging between 110 and 300 [12]. These scenarios are referred to as the HEO scenarios.

The performance of the L1-L2 filter, the L1-only filter, and the L1-only pointwise estimator are compared by examining specific Monte Carlo runs that stress the estimators in particular ways and by examining the statistical performance over all of the Monte Carlo runs. Four representative classes of scenarios are considered. The first class includes relatively short duration scenarios (several hours long) in which nothing unusual happens. Scenarios in this class will be referred to as "quiescent" scenarios. The second class includes short duration scenarios in which there is a significant change in the differential ionosphere on one or more of the channels. Such a change occurs when a GPS satellite is rising or setting behind the Earth. Scenarios in this class will be referred to as "ionosphere event" scenarios. The third class includes short scenarios that challenge the estimators' ability to converge and to remain locked onto the correct integer ambiguities. Differential ionosphere, poor GDOP, slow line-of-sight vector dynamics, and noisy measurements all may stress the estimators' convergence and robustness. Scenarios in this class will be referred to as "convergence/robustness" scenarios. The fourth class includes long duration scenarios lasting approximately one orbit, or 24 h in GEO and 38 h in HEO. Scenarios in this class will be referred to as "full orbit" scenarios.

The tuning parameters for the dynamics models are presented in Table 1. In the table, $\beta_{w_{AB}}$ is the common-mode process noise

Table 1 Tuning parameters in GEO and HEO scenarios

States	Symbols	L1-L2 filter	L1 filter	L1 pointwise
Spacecraft	$\beta_{w_{AB}}$, m^2/s^3	3×10^{-2}	3×10^{-2}	——
	$\beta_{\delta w_{AB}}$, m^2/s^3	5×10^{-7}	5×10^{-7}	——
Receiver clocks	h_0, m^2/s	$(7 \times 10^{-21}) \times c^2$	$(7 \times 10^{-21}) \times c^2$	——
	h_{-2}, m^2/s^3	$(2 \times 10^{-20}) \times c^2$	$(2 \times 10^{-20}) \times c^2$	——
Ephemeris errors	σ_e, m	1	1	1
	τ_e, s	20,000	20,000	20,000
TEC	$\sigma_{T_{\text{avg}}}$, m	5	——	——
	$\sigma_{T_{AB}}$, m	0.05	——	——
	τ_T, s	10	——	——

variance and $\beta_{\delta w_{AB}}$ is the differential-mode variance for the spacecraft orbital dynamics model. The terms h_0 and h_{-2} are typical Allen variances for a temperature compensated crystal oscillator. Next, σ_e is the steady-state standard deviation, and τ_e is the correlation time constant for the ephemeris error Markov model. The term $\sigma_{T_{\text{avg}}}$ is the common-mode steady-state standard deviation, $\sigma_{T_{AB}}$ is the differential-mode standard deviation, and τ_T is the correlation time constant for the TEC Markov model. The measurement error standard deviations are assumed to be $\sigma_P = 7$ m for the pseudorange and $\sigma_\phi = 0.01$ cycles for the carrier phase.

The performance of the estimators in a quiescent GEO scenario is illustrated in Fig. 4, which plots a 3.5 h time history of the three-dimensional relative position error components. The error components are expressed in a coordinate frame that is centered at one of the GPS receiver's antenna. Its axes point along the radial direction from the center of the Earth (radial), along the direction of motion (along track), and along the direction normal to the orbit plane (cross track). The plot shows that all three estimators perform well in this particular scenario. They all converge to the correct integer ambiguities in one measurement step, and navigate to subdecimeter-level accuracy or better. The L1-only pointwise estimator experiences maximum errors of about 5–7 cm, and the L1-only and L1-L2 filters experience maximum errors of about 2–3 cm. As expected, the filtered solutions are less noisy than the pointwise solution. The comparable performance of the L1-only filter and the L1-L2 filter is also expected given the fact that the differential ionosphere is negligible throughout the scenario. When the quiescent periods of 100 Monte Carlo runs are considered, the L1-only pointwise estimator has a mean error magnitude of 9.2 cm and a maximum error magnitude of 11.0 cm, the L1-only filter has a mean error magnitude of 1.1 cm and a maximum error magnitude of 6.0 cm, and the L1-L2 filter has a mean error magnitude of 1.2 cm and a maximum error magnitude of 6.0 cm.

All three estimators also perform well in the quiescent HEO scenarios. Figure 5 shows that, for a particular quiescent scenario, all the estimators converge to the correct integer ambiguities immediately. The L1-only pointwise estimator navigates to within about 1–1.5 m of the true relative position, and the filters, after some initial transients, navigate to within 20 cm of the truth. The relatively large errors in the filters' solutions over the first 0.5 h are due to the poor initial observability of the ephemeris error and TEC states. After a sufficient amount of data are processed, the Markov models converge, and the navigation errors settle to small values. Again, the L1-only and L1-L2 filters perform comparably when the effects of

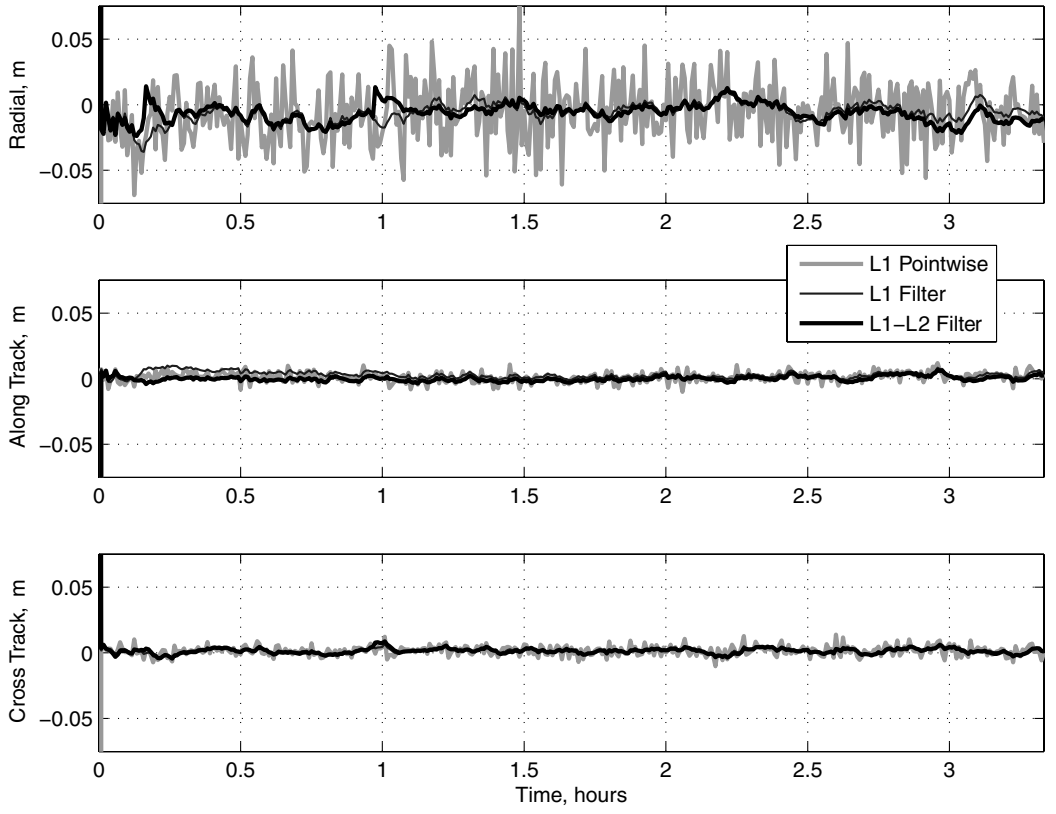

Fig. 4 Relative position error components in a quiescent GEO scenario.

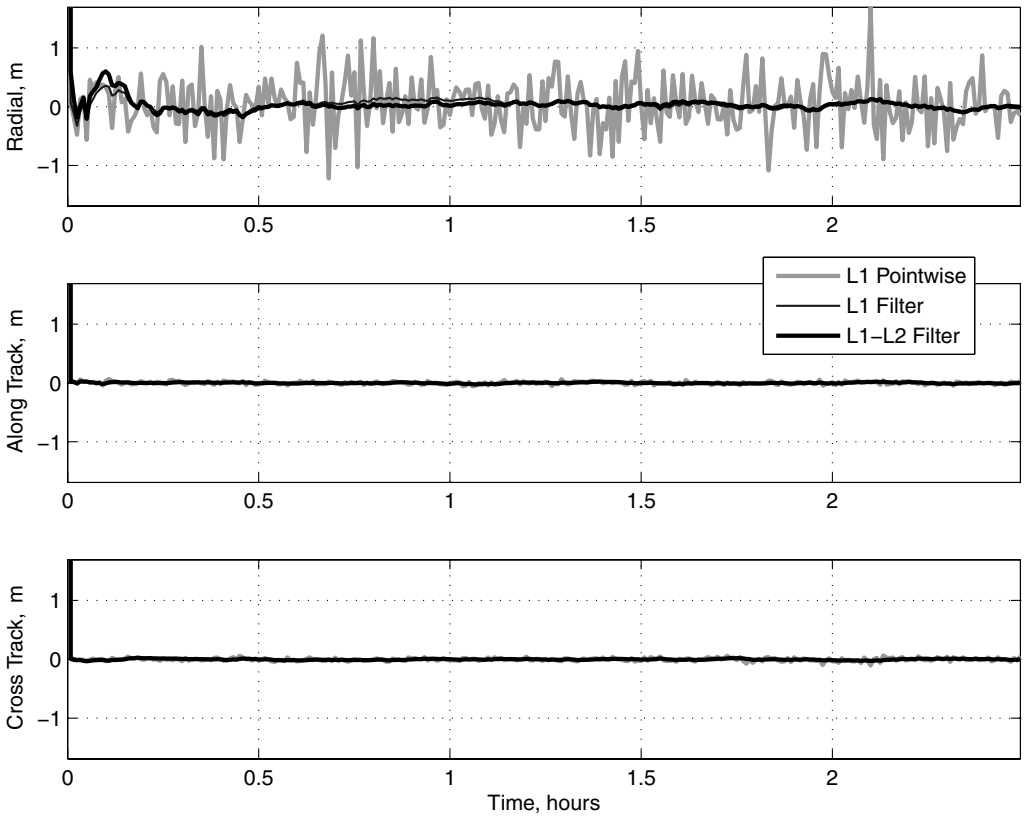

Fig. 5 Relative position error components in a quiescent HEO scenario.

differential ionosphere are negligible. When the quiescent periods of 100 Monte Carlo runs are considered, the L1-only pointwise estimator has a mean error magnitude of 13 cm and a maximum error magnitude of 5 m, the L1-only filter has a mean error magnitude of 13 cm and a maximum error magnitude of 54 cm, and the L1-L2 filter has a mean error magnitude of 11 cm and a maximum error magnitude of 54 cm. The quiescent scenario results are summarized in Table 2.

The performance of the estimators in a particular ionosphere event scenario is shown in Fig. 6 for the GEO formation. The L1-only filter and the L1-only pointwise estimator both show a significant increase in error about halfway through the scenario when one of the tracked GPS satellites sets behind the Earth. Moments before the signal is lost, the ray path dips into a dense portion of the ionosphere, increasing the absolute TEC experienced at each receiver and, more importantly, increasing the differential TEC experienced by the receivers. The latter effect is caused by the large TEC gradients to which the signal is subjected as it drops into the ionosphere. To get a better sense of how the signal interacts with the ionosphere, consider Fig. 7, which plots the orthogonal height of the setting satellite's ray path, a quantity that has been defined in Fig. 3. The ray path height drops from 7000 km above the Earth down to 350 km, the height at which the simulator drops the signal. That height is also the height of the densest portion of the simulated ionosphere. As the satellite sets, the pointwise estimator experiences a larger peak error, about 1 m, but recovers as soon as the signal is dropped. The L1-only filter has a smaller peak error, about 0.5 m, but takes longer to recover due to the averaging effects of filtering. The important result here, however, is that the dual-frequency filter successfully estimates the differential TEC and removes its effects. Its relative navigation solution shows no detectable degradation during the occultation. Considering the ionosphere events of 100 Monte Carlo runs, the L1-only pointwise estimator has a peak error magnitude of 2.03 m, the L1-only filter has a peak error magnitude of 1.99 m, and the L1-L2 filter has a peak error magnitude of 6 cm. Notice that the L1-L2 filter has exactly the same error magnitude as it had during the quiescent scenarios.

Table 2 Relative position error magnitudes for the quiescent scenarios

		L1 pointwise	L1 filter	L1-L2 filter
GEO	mean error, cm	9.2	1.1	1.2
	maximum error, cm	11.0	6.0	6.0
HEO	mean error, cm	43	13	11
	maximum error, cm	500	54	54

The performance of the navigation algorithms in the HEO scenarios during ionosphere events is similar to the performance in the GEO scenarios, with the exception that the magnitude of the errors is much larger. Considering the ionosphere events of 100 Monte Carlo runs, the L1-only pointwise estimator has a peak error magnitude of 28.70 m, the L1-only filter has a peak error magnitude of 4.41 m, and the L1-L2 filter has a peak error magnitude of 54 cm. Again, the L1-L2 filter's peak error magnitude identical to its quiescent scenario peak error magnitude. One could avoid the differential-ionosphere-induced navigation problems apparent in the L1-only estimators by discarding data from signals that pass too near the Earth. Those signals, however, are the strongest available at any given time and, therefore, are the easiest to acquire and track. Considering the difficulty of signal reception at high altitudes, one should hesitate before discarding any data. The ionosphere event scenario results are summarized in Table 3.

The convergence/robustness of the estimators is best illustrated by considering a particular HEO scenario that stresses the ability of the single-frequency estimators to estimate the correct integer ambiguities. Figure 8 shows a 60 min time history of the relative position error in such a scenario. Notice how the L1-only filter and L1-only pointwise estimator both take about 15 min to converge to the correct integers, whereas the L1-L2 filter takes less than 3 min to converge. This behavior, where one or both of the L1-only estimators converges slower than does the L1-L2 filter, occurs in 44% of the HEO Monte Carlo runs and can be attributed to ionosphere effects in most cases. In this particular scenario, however, the slow convergence cannot be attributed to the ionosphere because all of the ray paths are well above the dense portion of the ionosphere during the initial convergence period, as illustrated by the first 15 min

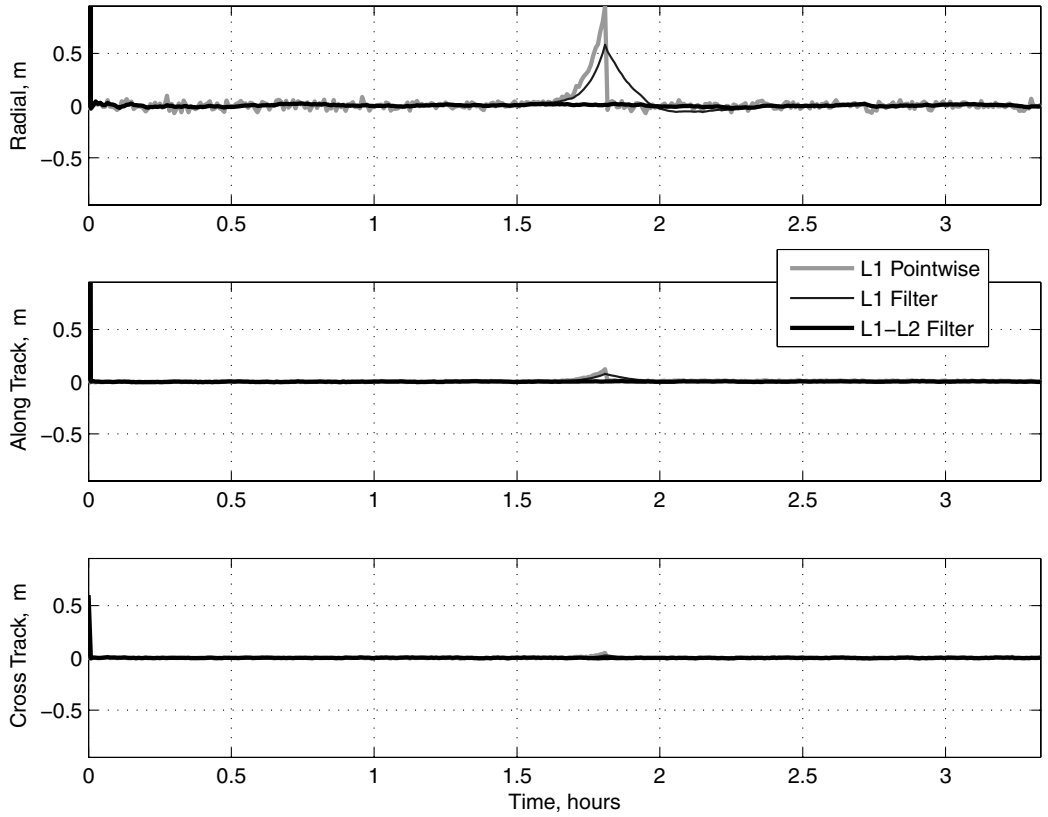

Fig. 6 Relative position error components in an ionosphere event GEO scenario.

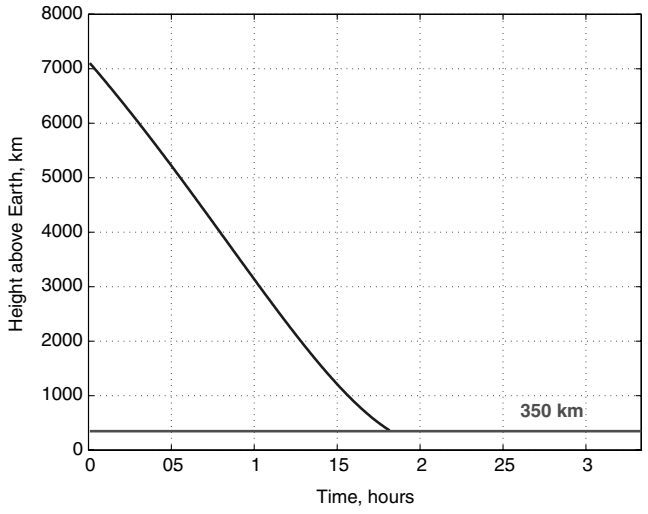

Fig. 7 Ray path height of a setting GPS satellite's signal.

of the graph in Fig. 9. This result indicates that, in the absence of ionosphere effects, the L1-L2 filter is using the dual-freqency measurements to aid in integer ambiguity resolution by performing implicit wide laning, rather than using the measurements to remove the effects of the ionosphere. The choice of how to best use the measurements can be made on a channel-by-channel basis, allowing the filter to use dual-frequency measurements to remove the effects of the ionosphere on some channels, while doing wide laning on other channels. This multimodal capability may account for the large improvements in convergence/robustness performance exhibited by the L1-L2 filter.

In the GEO convergence/robustness Monte Carlo runs, the L1-only pointwise estimator requires a mean of 1.06 30 s measurement steps to converge and requires a maximum of 51 steps, and the L1-only filter requires a mean of 1.59 steps and a maximum of 51 steps. The L1-L2 filter converges to the correct integer ambiguities in the first measurement step in all Monte Carlo runs. In the HEO runs, the L1-only pointwise estimator converges in mean of 9.4 30 s measurement steps and in two cases fails to converge in the 2.5 h scenarios. The L1-only filter converges in a mean of 10.5 steps and also fails to converge in two scenarios. The L1-L2 filter converges in a mean of 1.54 steps and a maximum of 11 steps. The convergence results are summarized in Table 4.

The robustness of the L1-L2 filter is highlighted again in the full orbit scenarios. Figure 10 shows one full orbit in a particular GEO scenario. The single-frequency estimators are relatively slow to converge to the correct ambiguities, and they experience large spikes in error periodically due to increases in the differential TEC that occurs when GPS satellites set. The dual-frequency filter converges immediately and experiences no degradation of the solution when satellites set.

The L1-L2 filter's robustness is also apparent in the full-orbit HEO scenarios. In these 38 h simulations, the formation satellites begin and end at an apogee distance of 18 Earth radii and pass through perigee distance of 1.2 Earth radii about halfway through the scenario. It is assumed that the formation satellites have nadir-pointing GPS antennas with hemispheric gain patterns throughout the orbit. This orientation gives good GPS visibility when the formation navigates above the GPS constellation, but poor visibility when it navigates at lower altitudes, especially near perigee. This assumption, which may be reasonable from an operational standpoint, has the effect of testing an estimation algorithm's ability to navigate through perigee with as few as four GPS signals, all of which are influenced by the ionosphere. Figure 11 shows the three

Table 3 Relative position error magnitude for the ionosphere event scenarios

		L1 pointwise	L1 filter	L1-L2 filter
GEO	maximum error, m	2.03	1.99	0.06
HEO	maximum error, m	28.7	4.41	0.54

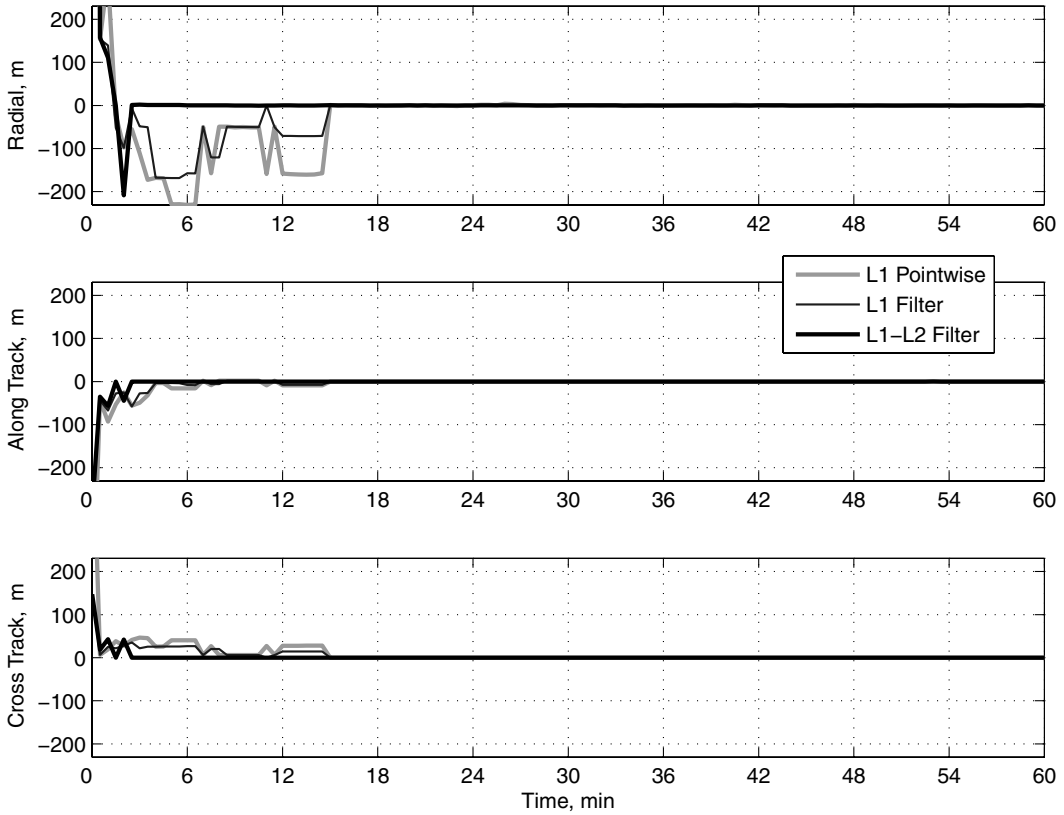

Fig. 8 Relative position error components for an HEO scenario that challenges the estimators' convergence capabilities.

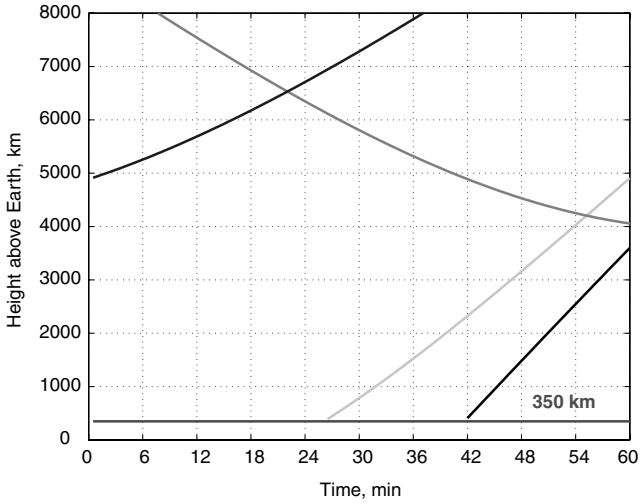

Fig. 9 Ray path height for several GPS satellites' signals during an HEO scenario that challenges the estimators' convergence capabilities.

estimators' relative position error components in a particular full-orbit HEO scenario. Both of the single-frequency estimators diverge from the correct integer ambiguity estimates and experience large navigation errors as the formation approaches perigee at 18.8 h. Here, the GPS satellite visibility drops briefly from 11 or 12 satellites to 4 satellites. About 40 min later, the number of tracked satellites returns to 11 or 12, but the estimators do not recover the correct integers until about 25.5 h in scenario time, or about 6 h after the good visibility is restored. The dual-frequency filter, on the other hand, remains converged throughout the entire orbit and experiences navigation errors of less than 20 cm, excluding the initial transients. Figure 12 shows a zoomed in version of the same results.

VI. Conclusions

A new dual-frequency CDGPS relative navigation filter has been developed for satellite formation flying at high altitudes. It uses dynamics models for the spacecraft orbits, receiver clocks, ionospheric TEC, and GPS satellite residual position and clock errors. The orbital dynamics are modeled with a 2×2 gravity model with sun and moon perturbations. The spacecraft state process noise is divided into two parts: one that is common to both satellites in the formation and another that acts differentially and that is much smaller in magnitude. Each receiver clock is modeled as evolving according to a two-state random walk/drift process. Both the GPS satellite ephemeris errors and the ionospheric TEC are modeled as evolving according to first-order Markov processes. The TEC variables are split into an average TEC between the receivers, which is allowed to experience relatively large changes, and a differential TEC, which is adaptively tuned to identify those instances in which this quantity is significant and those in which it is negligible. To this end, the differential TEC noise intensity scaling varies as a function of the receiver-Earth-transmitter relative geometry. The filter tracks undifferenced carrier phase ambiguities, thereby preserving information that is ordinarily discarded in CDGPS data processing, but it still uses the integer nature of the double-differenced ambiguities in the relative navigation solution by applying a LAMBDA-type method after the measurement update.

The L1-L2 filter's performance in Monte Carlo simulations has been compared with two other similarly designed CDGPS algorithms, an L1-only pointwise estimator and an L1-only filter.

Table 4 Number of 30-s measurement steps required to converge to the correct integer ambiguities

		L1 pointwise	L1 filter	L1-L2 filter
GEO	mean, steps	1.06	1.59	1
	maximum, step	51	51	1
HEO	mean, steps	9.4	10.5	1.54
	maximum, steps	>300	>300	11

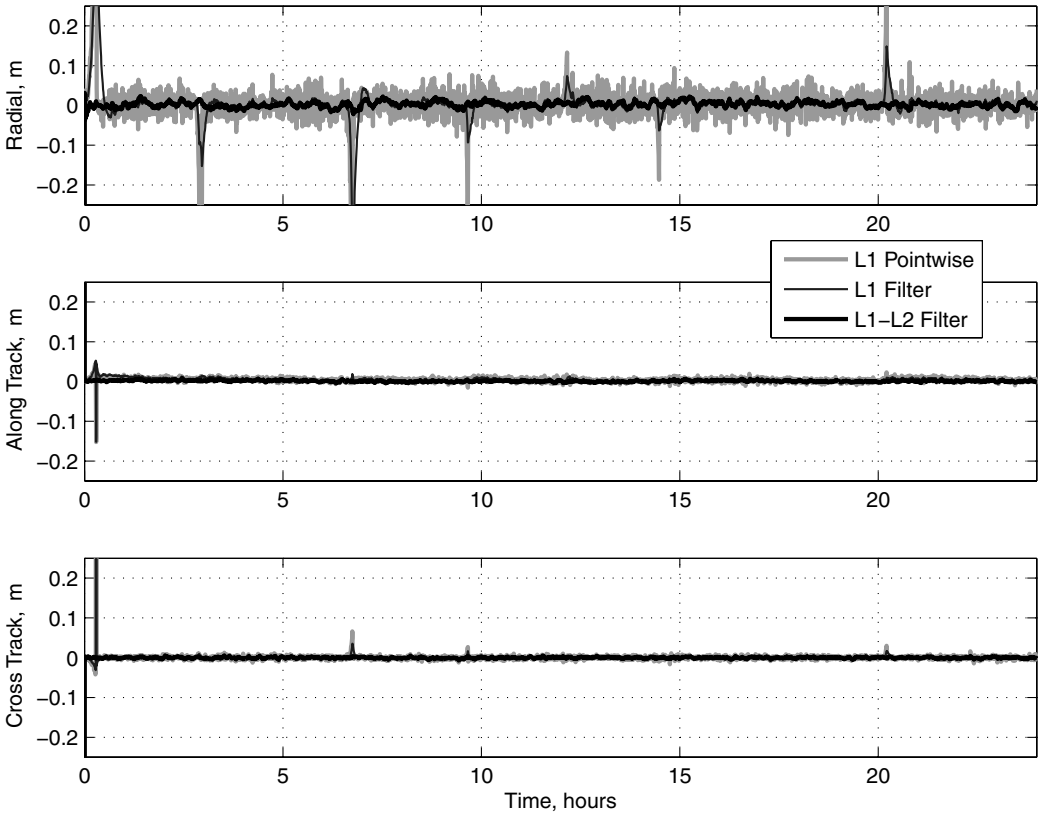

Fig. 10 Relative position error components for a full orbit in GEO.

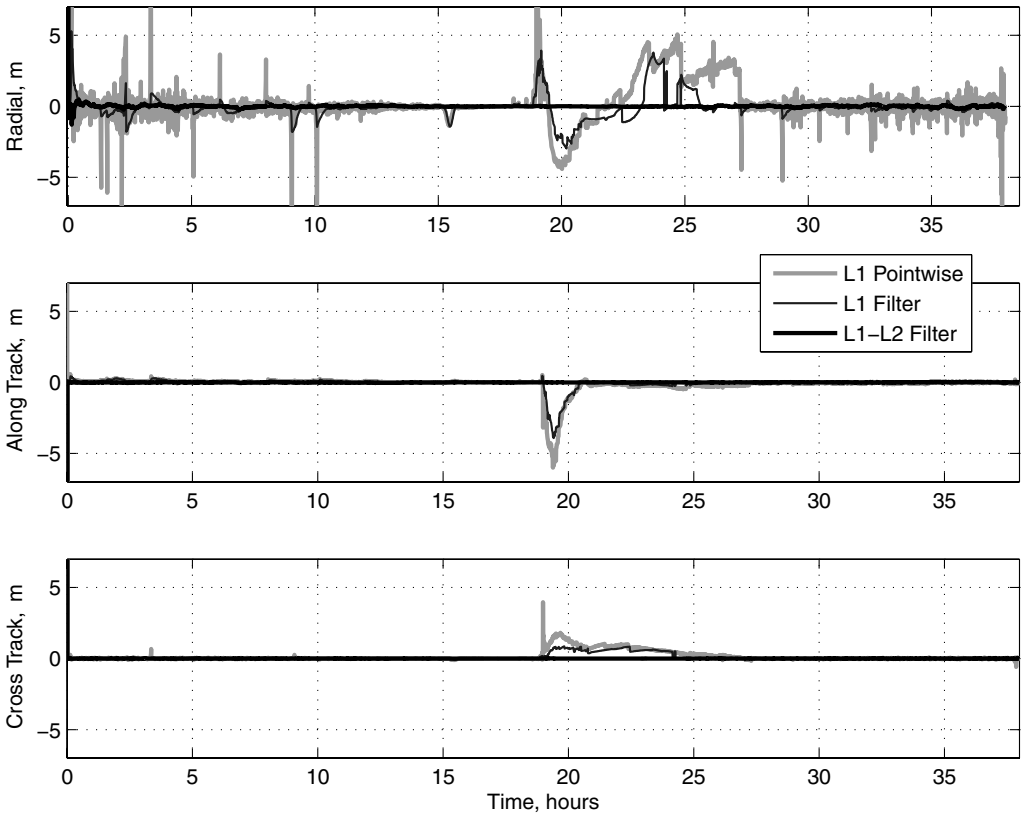

Fig. 11 Relative position error components for a full orbit in HEO.

The comparisons have focused on two template scenarios, a geostationary formation scenario and a high-Earth-orbit scenario. The filters are far less noisy than the pointwise estimator in the absence of significant differential ionosphere effects. Averaged over quiescent periods in all Monte Carlo runs, the filters both had average error magnitudes of less than 1.2 cm in GEO, compared with the pointwise estimator's 9.2 cm average. In HEO, the filters' mean error magnitudes were less than 13 cm, compared with the pointwise

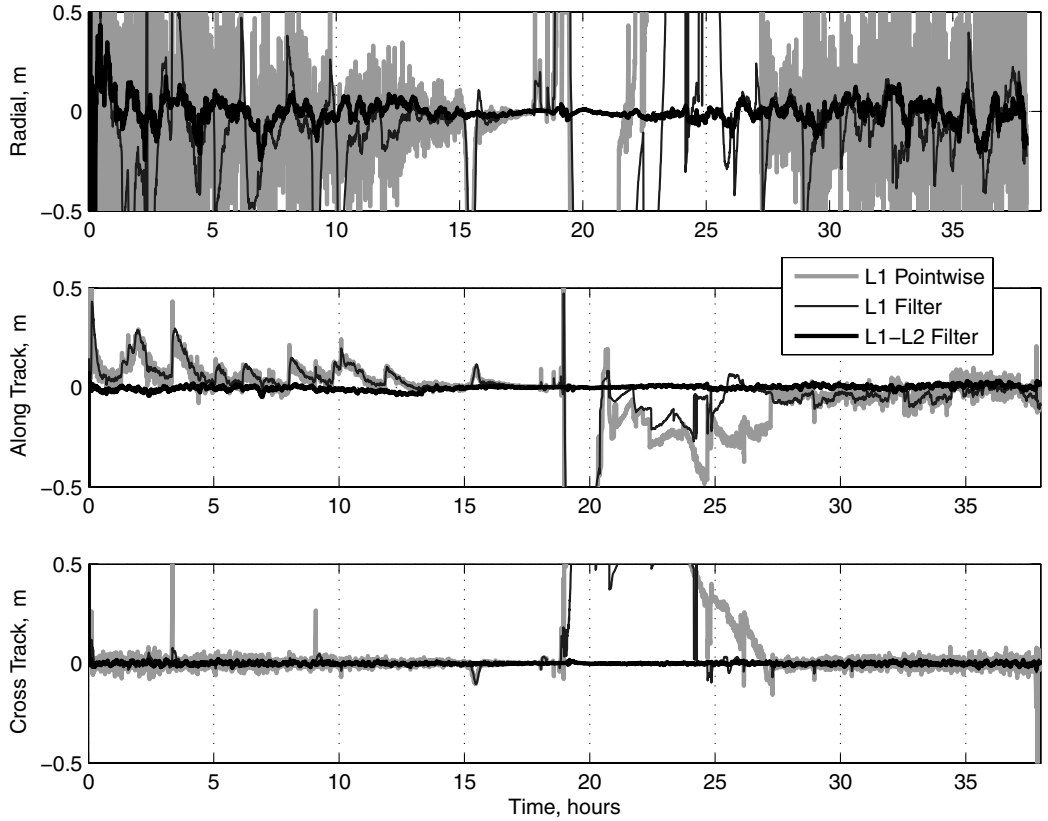

Fig. 12 Zoomed in version of the relative position error components for a full orbit in HEO.

estimator's 43 cm. The relative navigation results are significantly improved with the addition of filtering.

When the differential ionosphere becomes significant, the L1-L2 filter outperformed the single-frequency estimators. During ionosphere events, the dual-frequency filter accurately estimated and removed the effect of the differential TEC and experienced no discernible degradation in navigation accuracy. The single-frequency estimators, on the other hand, experienced large errors during the same events. The L1-only filter error magnitude reached 4.41 m and the pointwise estimator's error magnitude reached 28.7 m.

The L1-L2 filter also exhibited better convergence and robustness qualities than did the L1-only estimators. It converged to the correct integer ambiguity estimates faster than the other estimators in every Monte Carlo run and never diverged from the correct integers. These improvements can be partially attributed to the dual-frequency filter's ability to estimate and remove the effects of the differential ionosphere, but it also outperformed the other estimators in the absence of significant differential TEC. This latter behavior suggests that the L1-L2 filter can also use the dual-frequency measurements to aid in ambiguity resolution through implicit wide laning, and that, by considering the receiver-Earth-transmitter geometry, it is able to choose how to best use the measurements on a channel-by-channel basis.

References

[1] Montenbruck, O., Ebinuma, T., Lightsey, E. G., and Leung, S., "Real-Time Kinematic GPS Sensor for Spacecraft Relative Navigation," *Aerospace Science and Technology*, Vol. 6, No. 6, 2002, pp. 435–449.
doi:10.1016/S1270-9638(02)01185-9

[2] Kroes, R., and Montenbruck, O., "High Accuracy Kinematic Spacecraft Relative Positioning Using Dual-Frequency GPS Carrier Phase Data," *Proceedings of the 2004 ION NTM*, Inst. of Navigation, Fairfax, VA, Jan. 2004, pp. 21–31.

[3] Busse, F. D., How, J. P., and Simpson, J., "Demonstration of Adaptive Extended Kalman Filter for Low-Earth-Orbit Formation Estimation Using CDGPS," *Navigation: Journal of the Institute of Navigation*, Vol. 50, No. 2, 2003, pp. 79–94.

[4] Leung, S., and Montenbruck, O., "Real-Time Navigation of Formation-Flying Spacecraft Using Global-Positioning-System Measurements," *Journal of Guidance, Control, and Dynamics*, Vol. 28, No. 2, 2005, pp. 226–235.

[5] Kroes, R., Montenbruck, O., Bertiger, W., and Visser, P., "Precise GRACE Baseline Determination Using GPS," *GPS Solutions*, Vol. 9, No. 1, 2005, pp. 21–31.

[6] Psiaki, M. L., "FFT-Based Acquisition of GPS L2 Civilian CM and CL Signals," *Proceedings of ION GNSS 2004*, Inst. of Navigation, Fairfax, VA, Sept. 2004, pp. 457–473.

[7] Psiaki, M. L., and Jung, H., "Extended Kalman Filter Methods for Tracking Weak GPS Signals," *Proceedings of the 2002 ION GPS Conference*, Inst. of Navigation, Fairfax, VA, Sept. 2002, pp. 2539–2553.

[8] Mohiuddin, S., and Psiaki, M. L., "High-Altitude Spacecraft Relative Navigation Using Carrier-Phase Differential Global Positioning System Techniques," *Journal of Guidance, Control, and Dynamics*, Vol. 30, No. 5, 2007, pp. 1427–1436.
doi:10.2514/1.27827

[9] Psiaki, M. L., and Mohiuddin, S., "Relative Navigation of High-Altitude Spacecraft Using Dual-Frequency Civilian CDGPS," *Proceedings of the 2005 ION GPS Conference*, Inst. of Navigation, Fairfax, VA, Sept. 2005, pp. 1191–1207.

[10] Tapley, B. D., Schutz, B. E., and Born, G. H., *Statistical Orbit Determination*, Elsevier Academic Press, New York, 2004, pp. 160–172.

[11] Brown, R. G., and Hwang, P. A. C., *Introduction to Random Signals and Applied Kalman Filtering with Matlab Exercises and Solutions*, 3rd ed., Wiley, New York, 1977, pp. 428–431.

[12] Psiaki, M. L., and Mohiuddin, S., "Modeling, Measurement, and Simulation of GPS Carrier-Phase for Spacecraft Relative Navigation," *Journal of Guidance, Control, and Dynamics*, Vol. 30, No. 6, 2007, pp. 1628–1639.
doi:10.2514/1.29534

[13] Bierman, G. J., *Factorization Methods for Discrete Sequential Estimation*, Academic Press, New York, 1977.

[14] Gill, P. E., Murray, W., and Wright, M. H., *Practical Optimization*, Academic Press, New York, 1981, pp. 37–40.

[15] Psiaki, M. L., and Mohiuddin, S., "GPS Integer Ambiguity Resolution Using Factorized Least-Squares Techniques," *Journal of Guidance, Control, and Dynamics*, Vol. 30, No. 2, 2007, pp. 346–356.
doi:10.2514/1.21982

[16] Teunissen, P. J. G., Joosten, P., and Odijk, D., "Reliability of GPS Ambiguity Resolution," *GPS Solutions*, Vol. 2, No. 3, 1999, pp. 62–69.